

ABENICS: Active Ball Joint Mechanism With Three-DoF Based on Spherical Gear Meshings

Kazuki Abe^{ID}, Member, IEEE, Kenjiro Tadakuma^{ID}, Member, IEEE, and Riichiro Tadakuma^{ID}, Member, IEEE

Abstract—This article presents an active ball joint mechanism (ABENICS) enhanced by interactions of spherical gears. The gear-based joint drives three rotational degrees of freedom (RDoF) without slippage. The capabilities were inspired by the unique interactions between two different innovative gears [the cross spherical gear (CS-gear) and monopole gear (MP-gear)] and the superimposition of those interactions by the CS-gear’s quadrature spherical tooth structure. One MP-gear constrains two of the three RDoF of the CS-gear. The driving module which drives the MP-gear converts this “constraint” into a “drive” and drives the CS-gear with two RDoF. The CS-gear orthogonally superimposes the interactions caused by two MP-gears to achieve three RDoF driving forces. The principle was revealed by analyzing an equivalent linkage modeled on the mechanism of ABENICS. The linkage also led to the kinematics and torque equations. The theory and physical characteristics of ABENICS were verified in comprehensive and continuous positioning experiments on manufactured prototypes. The flexibility of the actuator placement was also verified in different configurations of the driving modules. The active ball joint, ABENICS can transmit high torque and reliable positioning in three RDoF without an orientation sensor, which applies to robot joints and orientation control mechanisms.

Index Terms—Development and prototyping, industrial robots, mechanism design, spherical gear.

I. INTRODUCTION

RESEARCH on multi-DoF mechanisms, actuators, and integrated robot joints has been ongoing, which is motivated by societal expectations. If multiple degrees of freedom (DoF) can be actuated in a single joint, robots will become smaller, less costly, or more functional than conventional robots.

Manuscript received July 31, 2020; revised December 23, 2020; accepted February 24, 2021. Date of publication April 26, 2021; date of current version October 1, 2021. This work was supported by the national project of the Program on Open Innovation Platform with Enterprises, Research Institute and Academia (OPERA) from the Japan Science and Technology Agency (JST) under Grant JPMJOP1614. This article was recommended for publication by Associate Editor Q. Li and Editor M. Yim upon evaluation of the reviewers’ comments. (*Corresponding author: Kazuki Abe.*)

Kazuki Abe and Riichiro Tadakuma are with the Department of Mechanical Systems Engineering, Yamagata University, Yamagata 9920038, Japan (e-mail: kazuki.abe.org@gmail.com; tadakuma@yz.yamagata-u.ac.jp).

Kenjiro Tadakuma is with the Graduate School of Information Science, Tohoku University, Sendai 980-8579, Japan (e-mail: tadakuma@rm.is.tohoku.ac.jp).

This article has supplementary material provided by the authors and color versions of one or more figures available at <https://doi.org/10.1109/TRO.2021.3070124>.

Digital Object Identifier 10.1109/TRO.2021.3070124

Over the years, numerous mechanisms and actuators that integrate multiple DoF in a single joint (contact surface) have been proposed. The classical mechanism, which uses friction for force transmission, comprises a sphere and several strategically placed friction wheels [1]–[4]. Although classical mechanisms allow unlimited motions with three rotational DoF (RDoF), their frictional losses are nonnegligible. In recent years, this problem has been solved by replacing the friction wheel with an omni wheel [5]–[7]. However, slippage prevents the effective transfer of high torque and precise positioning without external three-dimensional sensors. Another approach uses the high-frequency vibrations from piezoelectric or magnetostrictive elements [8]–[11]. These designs admit a wide velocity range and a compact design due to their simple construction, but they do not alleviate the above problems. Noncontact transmissive spherical actuators, which are three-dimensional extensions of induction or stepping motors, have also been proposed [12]–[25]. Although they provide a high-power capability, they consume large electrical and computational resources. Additionally, a gear reducer for outputting high torque at low speed is difficult to construct for these actuators. Instead of the spherical geometry, some researchers have proposed a linkage mechanism with a spherical linkage or a linkage consisting of a slider [26]–[32]. These mechanisms give high positioning accuracy and excellent dynamic characteristics because the actuators can be placed at the base of the system. However, physical interference between the links limits the motion range of the orientation. Especially with motions requiring three RDoF, achieving both range and stiffness is a challenging task [33].

A gear-based mechanism eliminates slippage and provides high torque and reliable transmission, but gear-based multiple RDoF mechanisms appear to be underrepresented in previous papers. Serial gear transmission mechanisms composed of differential bevel gears are often employed as the wrist/shoulder mechanism for robot arms [34]–[39], but their output capacity is restricted by the complex shaft nesting and the thrust load on a bevel-gear. Several parallel gear transmission mechanisms that superpose the tooth structures of different phases have also been proposed [40], [41]. These designs can potentially achieve high freedom of actuator placement, high stiffness, and high-torque transmission. However, driving three RDoF with a large motion range by such mechanisms has not been realized.

We have proposed various mechanisms and applications based on an omnidirectional driving mechanism with two DoF [42]–[45]. The mechanism combines two orthogonal tooth

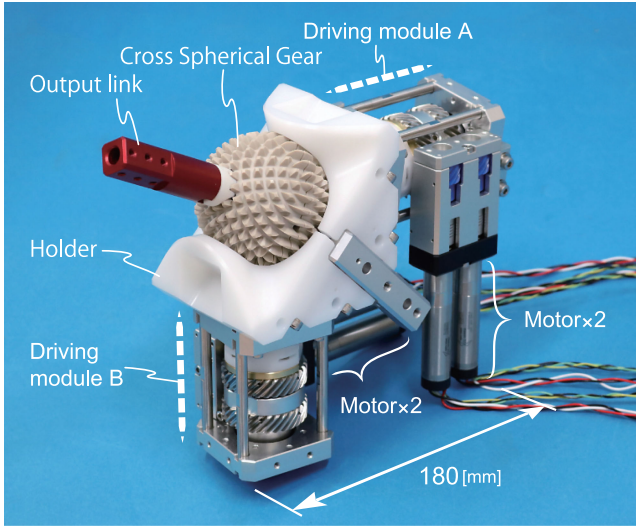


Fig. 1. Prototype of a new active ball joint mechanism, ABENICS.

structures to achieve a combination of two DoF: Orthogonal and linear, rotation and linear, and rotation and rotation.

This article proposes a new active ball joint mechanism (ABENICS) enhanced by interactions of spherical gears. ABENICS (Fig. 1) exploits the unique interactions between the innovative gears, namely, a cross spherical gear (CS-gear) and a monopole gear (MP-gear), to drive three RDoF without slippage. The CS-gear has a quadrature tooth structure engraved over the entire surface of a sphere, and the MP-gear is able to mesh with the CS-gear. Based on nonslip gear meshing, the mechanism provides high-torque transmission and reliable positioning without requiring a three-dimensional sensor. In addition, because the actuator and output link can be flexibly arranged, the mechanism can take various configurations. Nevertheless, its control system does not require much computational resource and electrical system. Although the proposed gears have complex shapes, we believe that recent advances in manufacturing technology will enable their practical fabrication. In optimized future designs, the mechanism will gather the joints of a robot at one point (i.e., at an active ball joint), reducing the energy and resource consumptions and improving the economy of robot operation.

This article describes the driving theory and control algorithm of ABENICS, and verifies and discusses the theory in a developed prototype. Section II describes the shape and interaction of the mechanism components and validates them with mechanical explanations. Section III describes the control algorithm of the mechanism, and Section IV presents the prototype designed through the theory. Section V experimentally verifies the characteristics of the mechanism and also discusses practical issues. Section VI concludes this article.

II. MECHANISM AND THEORY

The mechanism of ABENICS in Fig. 1 consists of a CS-gear supported by a holder and two driving modules of an MP-gear. The MP-gear has a unique tooth shape that meshes with the

CS-gear and is driven with two RDoF by the driving module. Thus, this mechanism is driven by four motors. If applied to a robot arm, the holder and the two driving modules are fixed to the same link \mathcal{B} on the root side, and the CS-gear is fixed to link \mathcal{H} on the end side. Consequently, the mechanism operates like an active ball joint with three RDoF between links \mathcal{B} and \mathcal{H} .

A. Mechanism

1) Cross Spherical Gear (CS-Gear): The CS-gear is formed by engraving two axisymmetric tooth structures on a spherical material. Specifically, the tooth structure is first engraved on the surface of the sphere around the x -axis like a lathe processing [Fig. 2 (b)]. This structure is based on the profile of an ordinary involute gear projected on the $x-y$ plane formed by the x - and y -axes. Next, by additionally engraving around the y -axis, a quadrature spherical tooth structure around both axes is formed on the spherical surface [Fig. 2 (c)]. In this article, the gears in panels (b) and (c) of Fig. 2 are called basic spherical gears and CS-gears, respectively. The central axis of a tooth structure is called a structural axis. The mechanism of ABENICS uses CS-gears, but basic spherical gears are sometimes used for convenience when explaining the principle of the mechanism.

The module m_{sph} of the involute tooth profile of the CS-gear is unconstrained. In contrast, the number of teeth z_{sph} is subjected to two constraints.

- 1) The number of teeth z_{sph} must be even.
($z_{\text{sph}} \in \text{EVEN}$).
- 2) The x and y -axes are located in the center of the valley or peak of the tooth.

These conditions are necessary to avoid obtaining incomplete teeth due to the interference of the two tooth structures and to mesh with the MP-gear, as described in Section II-A2.

The pitch circle diameter d_{sph} mm, the addendum circle diameter $d_{\text{a},\text{sph}}$ mm, and the tooth depth h_{sph} mm of a CS-gear are defined as follows, just like the typical spur gears:

$$d_{\text{sph}} = m_{\text{sph}} z_{\text{sph}} \quad (1)$$

$$d_{\text{a},\text{sph}} = d_{\text{sph}} + 2m_{\text{sph}} \quad (2)$$

$$h_{\text{sph}} = 2.25m_{\text{sph}}. \quad (3)$$

This idea of engraving tooth structures on a sphere has long been proposed as an improvement for universal joints [46]–[49]. Although multiple RDoF have been constructed from several planar [45] and basic spherical gear-like structures [40], [41], [44], an equivalent CS-gear engraved over the full surface of a sphere has not been previously reported.

2) Monopole Gear (MP-Gear): The MP-gears have a unique tooth structure, the pole, which can mesh with the CS-gears (Fig. 3). When the z - and x -axes are aligned with the rotational axis and the pole, an MP-gear is symmetric in the $x-y$ plane and its cross-section has a typical involute gear profile. The module m_{mpl} and number of teeth z_{mpl} of the profile are, respectively, given by

$$m_{\text{mpl}} = m_{\text{sph}} \quad (4)$$

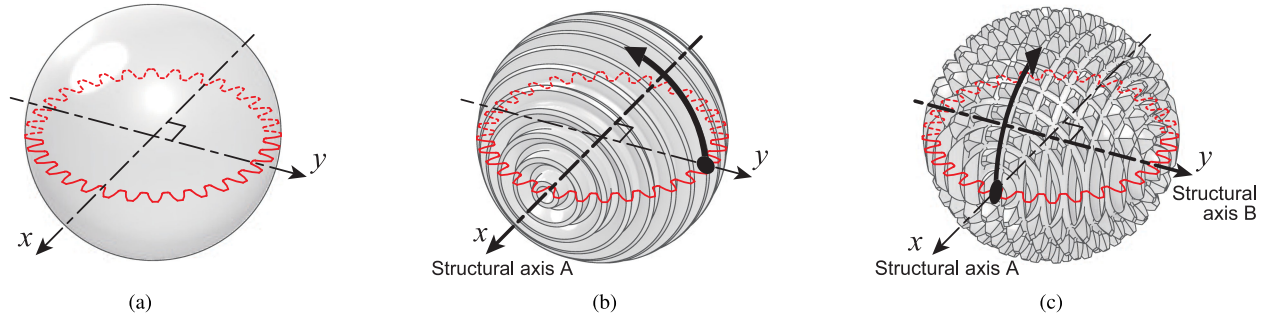


Fig. 2. Formation process of a CS-gear. (a) Material of the sphere before engraving the teeth. The $x-y$ plane showing the teeth profile includes the center point of the sphere. (b) Basic spherical gear, in which the tooth structure is formed around the x -axis (structural axis A). (c) Cross spherical gear, in which the tooth structure is formed around both structural axis A and the y -axis (structural axis B). (a) Material. (b) Basic spherical gear. (c) Cross spherical gear (CS-gear).

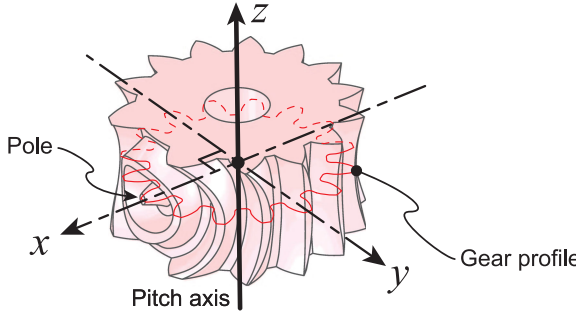


Fig. 3. Shape of the MP-gear. The x -axis is aligned with the pole, and the z -axis is aligned with the pitch rotation axis.

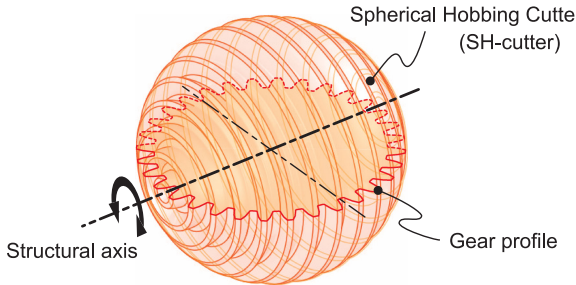


Fig. 4. SH-cutter used for sharpening. The SH-cutter is shaped like a rotating body with a gear profile around the structural axis.

$$z_{\text{mpl}} = \frac{z_{\text{sph}}}{2}. \quad (5)$$

Taking advantage of the repeated shape of CS-gear, MP-gear becomes smaller, i.e., one pole of the MP-gear can correspond to two poles of the CS-gear.

To explain the tooth structure of the MP-gear, the spherical hobbing cutter (SH-cutter) (Fig. 4) is shaped similarly to a basic spherical gear [Fig. 2 (b)] and is formed by rotating a typical gear profile around a structural axis.¹ Like a standard hobbing cutter, the SH-cutter engravés the tooth structure by pressing the pattern into the material. For simplicity, we describe the SH-cutter by its structural axis and gear profile hereafter.

¹More accurately, the tooth addendum and dedendum need to be adjusted.

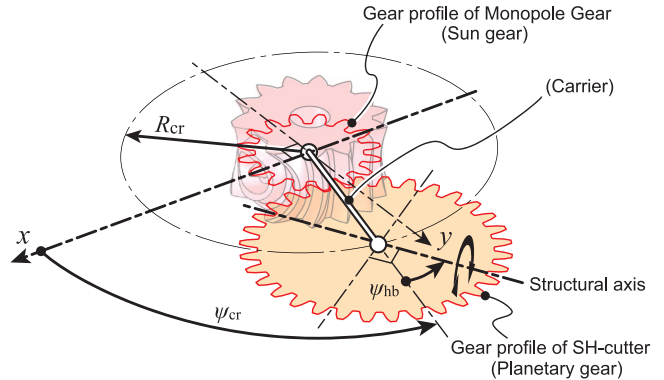


Fig. 5. Hobbing process of a MP-gear. The gear profiles of the MP-gear and SH-cutter mesh and collectively behave like a planetary gear mechanism with a sun gear, planetary gear, and carrier. The material placed in the center is continuously sharpened by the SH-cutter. The SH-cutter is symmetric about a structural axis (omitted here; see Fig. 4). Note that the angle of rotation of the planetary gear is expressed as a relative angle to the carrier.

The gear profiles of the MP-gear and SH-cutter are arranged on the same plane and mesh like a typical pair of spur gears (Fig. 5). If the distance between the centers is fixed at some appropriate length, the system behaves as a planetary gear mechanism. The length of the carrier R_{cr} mm, the revolution angle of the planetary gear ψ_{cr} rad around the sun gear, and the rotation angle of the planetary gear ψ_{hb} rad are, respectively, defined as follows:

$$R_{\text{cr}} = \frac{m_{\text{sph}}(z_{\text{sph}} + z_{\text{mpl}})}{2} = \frac{m_{\text{sph}}}{2} \frac{3z_{\text{sph}}}{2} = \frac{3}{4} d_{\text{sph}} \quad (6)$$

$$\psi_{\text{hb}} = \frac{\psi_{\text{cr}}}{2} (0 \leq \psi_{\text{cr}} < 2\pi). \quad (7)$$

Note that in the initial state, the x -axis is assumed to be aligned with the structural axis.

Now, we suppose that the material of the MP-gear is placed at the center of the $x-y$ plane. As the orbital revolution angle ψ_{cr} continuously increases from 0 rad to 2π rad, the SH-cutter rotates around the material like a planetary gear while also cutting the material. As the SH-cutter revolves around the material,

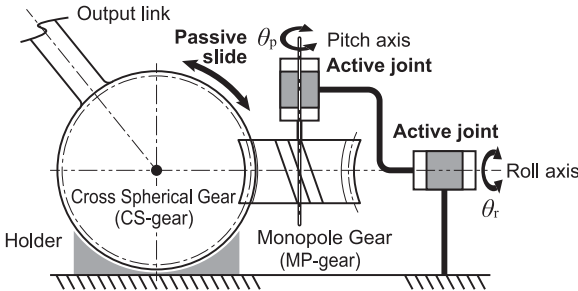


Fig. 6. Skeleton model of the driving module. The MP-gear is driven by two active joints, providing two RDoF. A passive slide between the CS-gear and the MP-gear (indicated by the arrow) provides another RDoF. This slide is generated when the pole of the MP-gear is directed to the right side of this figure.

the structural axis rotates as described by (7). This process is essential for meshing the MP-gear with the CS-gear.

As the two poles of the basic spherical gear are symmetrical, an MP-gear with half the number of teeth and only one pole can unlimitedly mesh with the basic spherical gear. This behavior appears to draw a polar orbit with respect to the CS-gear.² Moreover, an MP-gear can mesh not only with the basic spherical gears but also with the CS-gears possessing two structural axes [Fig. 2 (c)].³

The large tooth width of the MP-gear effectively constrains the CS-gear, thus stabilizing “coupling motion.”⁴ The tooth width is determined by considering the size of the “Driving module” (see Section II-A3).

3) Driving Module: When assembled into a differential mechanism, the MP-gear can drive the CS-gear. In this article, the MP-gear driving system is defined as the driving module.

The driving module uses two actuators and outputs two RDoF, roll θ_r and pitch θ_p of the MP-gear. The skeleton of the equivalent linkage is shown in Fig. 6. The roll axis intersects with the centers of an MP-gear and CS-gear, and the pitch axis coincides with the z -axis of Fig. 3. The driving module is essentially a two-axis gimbal mechanism with its pitch axis adjacent to its roll axis. Our prototype model replaces this equivalent linkage with a differential mechanism.

ABENICS requires two driving modules. Most importantly, each MP-gear must mesh with one of the two tooth structures of the CS-gear. For example, Fig. 7 shows the two tooth structure based on the structural axis A and B of CS-gear meshing with the MP-gear of driving module A and B, respectively. This mechanism enables the CS-gear/output link to be driven with three RDoF.

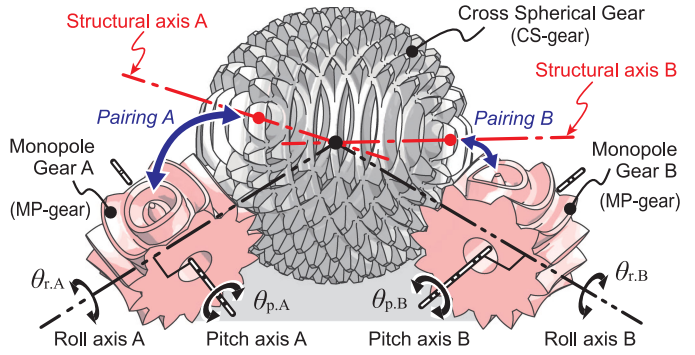


Fig. 7. View of the two tooth structures and their respective pairings with the two monopole gears (MP-gears). Each MP-gear is driven by a driving module. Note that the orientation of the pitch axis is affected by the rotation around the roll axis.

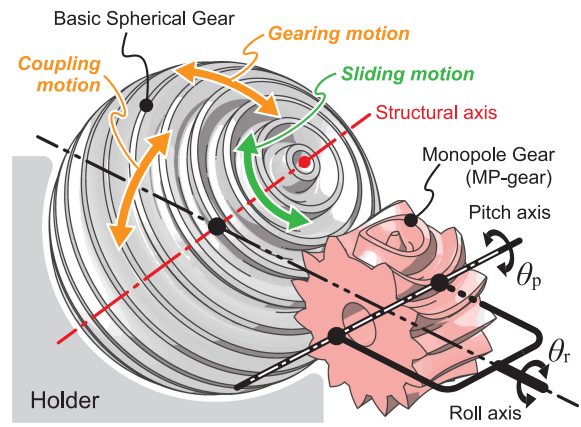


Fig. 8. Three motions are invoked by the interaction between the MP-gear and the CS-gear.

B. Theory

This section shows how the interaction between the components of the ABENICS mechanism can drive three RDoF.

1) Three Motions Invoked by Gear Interaction: The interaction between a CS-gear and an MP-gear generates gearing, coupling, and sliding motions. In Fig. 8, these three motions are invoked by a basic spherical gear [Fig. 2 (b)] and an MP-gear.

As the MP-gear rotates around the pitch axis, its teeth mesh with those of the CS-gear, and the driving force is transferred from the MP-gear to the CS-gear (this behavior resembles that of a spur gear). The coupling motion transmits the driving force through the roll rotation of the wide-toothed MP-gear, similarly to Oldham’s shaft coupling. The sliding motion caused by passive slippage of the tooth surface does not transfer the driving force.

When the poles of the CS-gear and MP-gear are coincident, the roll rotation of the MP-gear does not transmit any torque. However, the torque direction of the gearing motion can be freely chosen there, just like a steering motion in a car.

If the MP-gear in Fig. 8 is fixed, the interaction of the three motions constrains all motions except the rotation around the

²Such an orbit describes the path of a satellite passing over the Earth’s north and south poles.

³A CS-gear [Fig. 2 (c)] is composed of two tooth structures engraved around two structural axes. In other words, two orthogonal basic spherical gears coexist [Fig. 2(b)].

⁴“Coupling motion” is one of the motions invoked by the interaction between the CS-gear and MP-gear. For more information about these three motions and interactions, see Section II-B1.

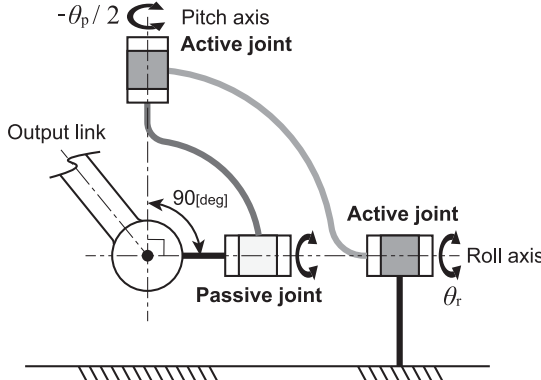


Fig. 9. Skeleton view of a MP-gear with a driving module expressed as an equivalent linkage. The output link has the equivalent capability as the mechanism of the driving module in Fig. 6. For a more accurate comparison between the figures, the axis of the passive joint should be perpendicular to the paper surface. The amount of rotation of the pitch axis is half that of Fig. 6 and the direction is opposite.

structural axis. In other words, a single MP-gear can constrain or drive two of the three RDoF of the CS-gear.

A CS-gear with two crossed-tooth structures [Fig. 2 (c)] can superimpose the interactions of two MP-gears. One MP-gear that meshes with the tooth structure of the structural axis A constrains the CS-gear's rotations except for the rotation around the structural axis A. Similarly, the other MP-gear constrains the rotations except around the structural axis B. Because structural axes A and B are orthogonal, the two MP-gears can constrain or drive all RDoF of the CS-gear. This fact is clarified in a mechanical analysis in the next section.

2) Equivalent Linkage and Number of Degrees of Freedom: Based on the interactions described in Section II-B1, Fig. 6 is replaced with the linkage mechanism shown in Fig. 9, i.e., the relationship between the CS-gear and the two driving modules can be expressed by the equivalent closed linkage shown in Fig. 10. This linkage satisfies the following two conditions.

- 1) The axes of rotation of all six joints intersect at the center O of the CS-gear.
- 2) The angle between the axes of any two joints (but without the angle between two joint axes on the ground) is 90 [deg].

This closed-linkage mechanism is a type of spatial mechanism that becomes an overconstrained spherical mechanism under the condition (1). Therefore, from Gruebler's equation, the number of DoF is given by

$$F = 3(N - J - 1) + \sum_{i=1}^J f_i \quad (8)$$

where N is the number of links, J is the number of joints, and f_i is the DoF of the i th joint. In Fig. 10, suppose that $N = 6$, $J = 6$, and $f_{1\ldots 6} = 1$. The number of DoF of this equivalent linkage is $F = 3$, meaning that the output link in Fig. 10 has three RDoF.

We now focus on one of the driving modules in Fig. 10, i.e., the link consisting of A_1 , A_2 , and A_3 . This module is an RR-type

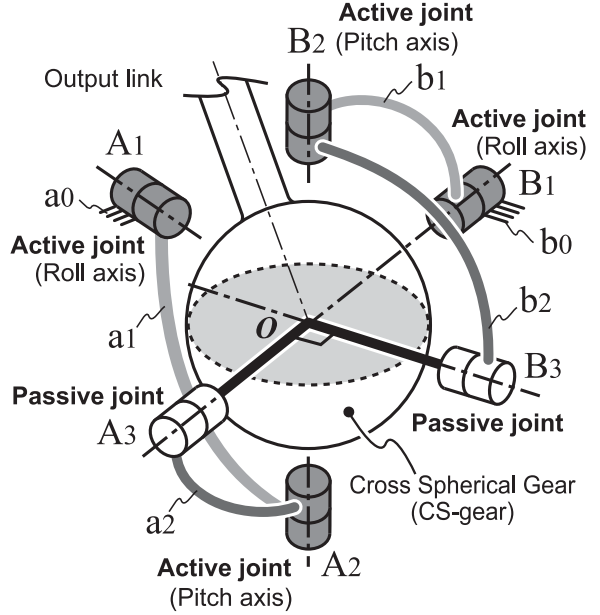


Fig. 10. Skeleton model of a new ABENICS represented by an equivalent linkage. This parallel linkage mechanism is composed of the two mechanisms shown in Fig. 9. The output link achieves a driving torque with three RDoF.

two-link serial arm with the passive joint A_3 as the end-effector. As the linkage is spherical, the end-effector A_3 has two DoF on the spherical surface centered at O . The same description holds for the other driving module. Therefore, the CS-gear can be considered driven in parallel by two serial arms. Since each arm is connected to the CS-gear via a passive joint and all joints are orthogonal, the output link acquires three RDoF.

Interestingly, this equivalent linkage suggests that the capability of the ABENICS mechanism is independent of the positions of joints A_1 and B_1 , i.e., the relative angle between the driving modules need not be 90 [deg]. For example, the modules can oppose each other along a straight line.

As shown in Fig. 10, the possible orientation angles of the output link in a manufactured equivalent linkage are limited largely by mechanical interference between the links. Accordingly, one of the most significant achievements of this study is the realization of unlimited motion range by replacing this equivalent link with a gear-based mechanism of ABENICS.⁵

III. CONTROL ALGORITHM

In this section, the ABENICS mechanism is modeled more abstractly and the generalized inverse kinematics is derived. The more detailed forward/inverse kinematics and torque relationship equations are described in Appendix C. The model uses the target rotation angle r, p, y rad of the CS-gear and the orientation $\alpha_n, \beta_n, \gamma_n$ rad of both driving modules ($n = A, B$), and outputs the pitch and roll rotation angles $\theta_{r,A}, \theta_{p,A}, \theta_{r,B}, \theta_{p,B}$ rad of

⁵ Although the output link points outward Fig. 10 it can also be regarded as a structure inside the CS-gear. In this case, the orientation angle of the CS-gear is unrestricted.

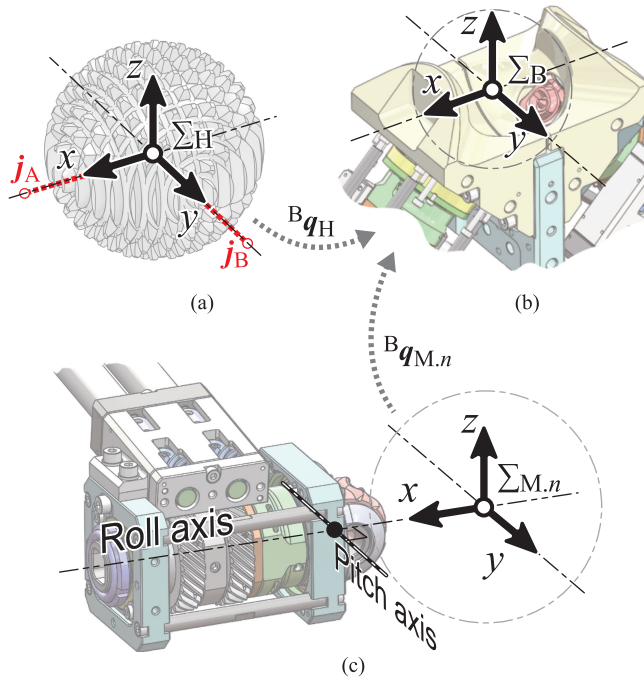


Fig. 11. Definitions of the coordinate systems. (a) Cross spherical gear (CS-gear). (b) Holder/Base. (c) Driving module.

the two MP-gears. This article assumes the right-hand coordinate system and XYZ-Euler angles.

A. Definitions

Three coordinate axes are defined in this mechanism: The Σ_B world coordinate system fixed at the holder, the Σ_H local coordinate system fixed at the CS-gear, and the $\Sigma_{M,n}$ ($n = A, B$) local coordinate system fixed at the driving module. The coordinate systems of the driving modules A and B are separately defined as $\Sigma_{M,A}$ and $\Sigma_{M,B}$, respectively, giving four coordinate systems in total. As only rotation is considered here, the origin points $O_B, O_H, O_{M,n}$ of all coordinate systems coincide. These coordinate systems are shown in Fig. 11.

The derivation of the algorithm involves two types of coordinate transformations: A transformation Bq_H showing the relative orientations of Σ_B and Σ_H and a transformation $Bq_{M,n}$ showing the relative orientations of $\Sigma_{M,n}$ and Σ_B .

Because Bq_H is the target orientation of the CS-gear, it is expressed as the following function of r, p , and y rad:

$$Bq_H = R(r, p, y) \quad (9)$$

where R is the rotation matrix.

Moreover, as $Bq_{M,n}$ is the orientation of the driving module with respect to Σ_B , it is expressed as the following function with mechanical constants $\alpha_n, \beta_n, \gamma_n$ rad:

$$Bq_{M,n} = R(\alpha_n, \beta_n, \gamma_n). \quad (10)$$

Based on these definitions, the control algorithm is derived as below.

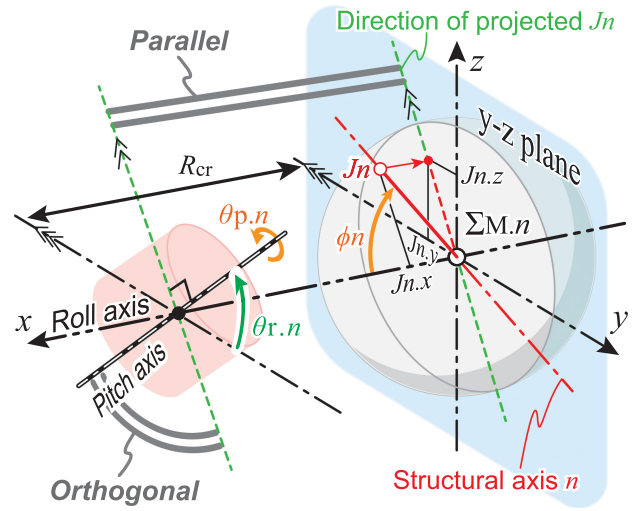


Fig. 12. Schematic of the control theory. The variable $\theta_{p,n}$ in the MP-gear is derived from the angle ϕ_n between J_n and the x -axis of $\Sigma_{M,n}$. The variable $\theta_{r,n}$ is derived from the angle between J_n and the z -axis projected onto the y - z plane.

B. Algorithm

To derive the inverse kinematics of this mechanism, we require two unit vectors j_A and j_B extending from the origin O_H in Σ_H . These vectors determine the directions of the two structural axes [Fig. 11 (a)] as follows:

$$j_A = \begin{bmatrix} j_{A,x} \\ j_{A,y} \\ j_{A,z} \end{bmatrix} = \begin{bmatrix} 1 \\ 0 \\ 0 \end{bmatrix} \quad (11)$$

$$j_B = \begin{bmatrix} j_{B,x} \\ j_{B,y} \\ j_{B,z} \end{bmatrix} = \begin{bmatrix} 0 \\ 1 \\ 0 \end{bmatrix}. \quad (12)$$

Next, the coordinates of the unit vectors j_n ($n = A, B$) are transformed by Bq_H and the inverse matrix of $Bq_{M,n}$, obtaining unit vectors J_n in the coordinate systems $\Sigma_{M,n}$ of the driving modules

$$J_n = (Bq_{M,n})^{-1} Bq_H j_n. \quad (13)$$

Here, when the vector J_n is projected onto the y - z plane in $\Sigma_{M,n}$, the projected vector and the pitch axis of the driving module n must be directed orthogonally to each other around x axis, as shown in Fig. 12. Therefore, the roll angle $\theta_{r,n}$ is given by

$$\theta_{r,n} = \tan^{-1} \left(\frac{J_{n,y}}{J_{n,z}} \right) \quad (14)$$

where $\tan^{-1}(J_{n,y}/J_{n,z})$ is calculated by the inverse tangent function ATAN2(y,x) provided in most programming languages, specifically ATAN2($J_{n,y}, J_{n,z}$). This calculation obtains the angle between the position vector $J_{n,y}, J_{n,z}$ and the z -axis. Note that when $J_{n,y}$ and $J_{n,z}$ are both zero, equation (14) does not provide the solution. In this case, exception handling is performed, such as reusing the previous angle value.

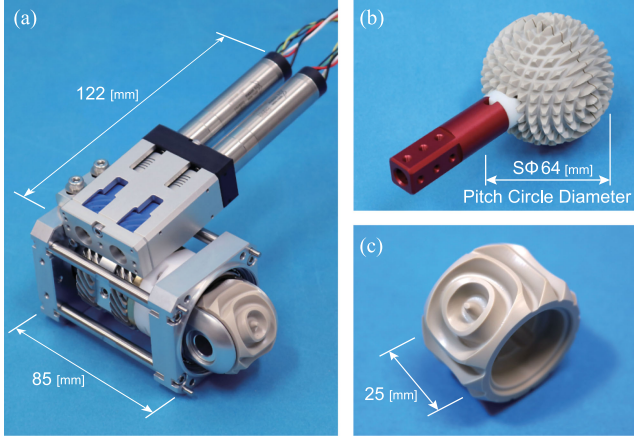


Fig. 13. Main components of the manufactured prototype. (a) Driving gear. (b) CS-gear and output link. (c) MP-gear.

The angle between the vector \mathbf{J}_n and the x -axis in the ${}^B\mathbf{q}_{M,n}$ is obtained as follows:

$$\phi_n = \cos^{-1}(J_{n,x}). \quad (15)$$

By (5) giving the tooth ratio of the CS-gear and an MP-gear, the pitch angle $\theta_{p,n}$ is given by

$$\theta_{p,n} = 2\phi_n = 2\cos^{-1}(J_{n,x}). \quad (16)$$

These calculations generate the angles $\theta_{r,n}$ and $\theta_{p,n}$ of the two RDoF of an MP-gear. In practice, the rotation angles of the four motors are determined by the effect of the differential unit and their respective reduction ratios.

C. Actuation Redundancy

In this article, the mechanism principle is revealed using simple position-velocity control with MP-gear target angles. On the other hand, ABENICS is an overactuated mechanism, thus in practice, those joint angles and torques need to be distributed strategically.

In this mechanism, one of the four active joints can be regarded as following the others. This relational equation for joint angles is shown in Appendix C-A. Furthermore, the torques of the joints are also considered to affect each other. The relationship between these torques is described in Appendix C-C.

These increase the complexity of the control algorithm, but also bring the possibility to enhance the stiffness of the joint. By referring to the torque relationship and controlling the torque of the motors, this mechanism is expected to work more effectively.

IV. PROTOTYPE

The theory developed in Section II is verified in a prototype of ABENICS (Figs. 1 and 13). This section presents the concept, mechanical design, and control system of the prototype.

A. Design Concept and Requirements

The specifications of the CS-gear in the prototype are shown in Table I. In determining the mechanical parameters, it is assumed

TABLE I
SPECIFICATIONS OF THE CROSS SPHERICAL GEAR IN THE PROTOTYPE

Parameter	Value	Unit
Standard torque	400	mN·m
Standard rotational speed	1.0	rot/s
Standard acceleration	5.0	rot/s ²
Motion range without output link	no limit	deg
Motion range (roll axis)	$\pm 90^a/\pm 135^b$	deg
Motion range (pitch axis)	$\pm 45^a/\pm 45^b$	deg
Motion range (yaw axis)	No limit	deg
Angle between the driving modules	$90^a/180^b$	deg

^a Perpendicular type.

^b Opposite type.

that a rod of length 300 mm and weight 0.5 kg is connected to the output link. The CS-gear's motion range allowed by the output link depends on the opening area of the holder. The contact surface area between the holder and the CS-gear is an important stabilizing factor in the mechanism of ABENICS. Considering this factor in our design, we widened the motion range of the CS-gear.

In this study, the angle between the two driving modules was varied as 90 [deg] and 180 [deg]. However, this angle can be arbitrarily set as described in Section II-B2. In addition, the CS-gear and MP-gear modules and the number of teeth can also be set arbitrarily as long as the conditions are met. In other words, the size and design values of this prototype are one of the possible forms of ABENICS.

B. Mechanical Design

Following the design concept, this study developed a prototype of the ABENICS mechanism. The computer-aided design model of the perpendicular-type prototype is shown in Fig. 14. The holder attached to the base plate holds the CS-gear like a ball joint. Both driving modules are connected to the holder. Each driving module has a differential unit for pitch and roll rotations of the MP-gear that meshes with the CS-gear. This unit is composed of an inner rotor, a differential inner worm gear, a differential pinion, and the MP-gear. The inner rotor is rotated around the roll axis by the roll driving motor. The differential inner worm gear that has teeth inside the cylinder is rotated around the same axis by the pitch driving motor. The differential pinion installed on the inner rotor transmits the force to the MP-gear caused by the rotational speed difference between the inner rotor and the inner worm. The MP-gear installed on the inner rotor obtains the driving force of the rotation around the roll axis and the pitch axis from the inner rotor and the differential pinion, respectively. Note that the orientation of the pitch axis is affected by the rotation around the roll axis. This driving module also has an ability to adjust the distance or backlash between the CS-gear and the MP-gear, which consequently corrects manufacturing and assembly errors.

The differential unit enables the attachment of all four motors to the base. However, the large difference between the reduction ratios of the roll and pitch rotations creates an asymmetric

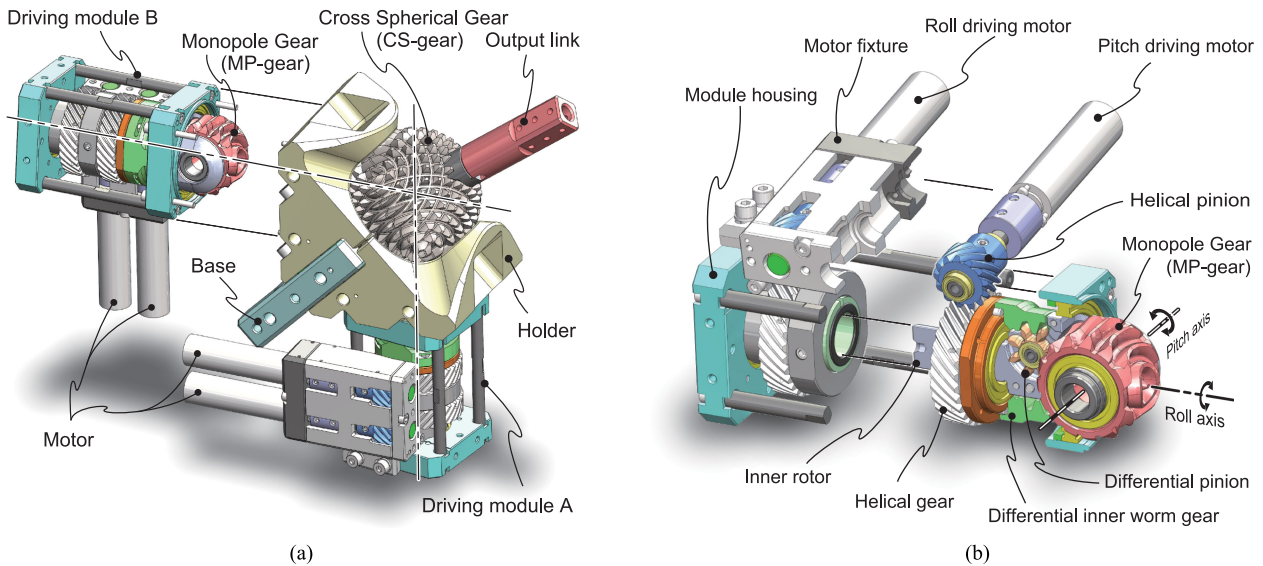


Fig. 14. Prototype of the new ABENICS. (b) Two driving modules are installed in (a) one prototype. The base supports the whole device and the output link provides the driving force. The dotted lines are auxiliary lines indicating that the parts are disassembled. In (b), part of the driving module is removed to show the internal structure. (a) Design of the ABENICS mechanism. (b) Design of the driving module.

TABLE II
SPECIFICATIONS OF THE SPHERICAL AND MONPOLE GEARS

Parameter	cross spherical gear (CS-gear)	monopole gear (MP-gear)	Unit
Quantity	1	2	-
Module of gears	2.0	2.0	mm
Number of gear teeth	32	16	-
Pitch diameter	64.0	32.0	mm
Addendum diameter	68.0	-	mm
Rack shift	0.0	-0.1	mm
Width	-	20	mm
Profile of teeth	involute	involute	-

TABLE III
SPECIFICATIONS OF MOTORS

Parameter	Pitch motor	Roll motor	Unit
Quantity	2	2	-
Type	BLDC ^a	BLDC	-
Power capacity	48.5	48.5	W
Operating voltage	24	24	V
Sensor resolution	8192	8192	pulse/rot
Reduction ratio	19/75	10/66	-
Total reduction ratio ^b	247/36000	13/198	-

^a BLDC: Brushless DC motor.

^b Ratio of rotational speeds of the motor's rotor and the CS-gear.

backlash on the MP-gear.⁶ Moreover, the driving module of this prototype is more elongated than necessary to verify multiple forms.

1) *Gear Design and Motor Selections:* Table II lists the specifications of each gear and Table III summarizes the performance of the selected motor. The CS- and MP-gears satisfy the

⁶See total reduction ratio in Table III

TABLE IV
MATERIALS OF THE MAIN PARTS

Parts	Material	Annotation
Cross Spherical Gear	PEEK ^a	Normal grade
Monopole gear	PEEK	Normal grade
Holder	POM ^b	-
Differential pinion	C3604 ^c	-
Differential inner worm	POM	-
Helical gear	SUS303	-
Helical pinion	MC nylon	-
Module housing	A2017 ^d	Anodized
Base	A2017	Anodized

^a PEEK: Polyetheretherketone.

^b POM: Polyoxymethylene.

^c Brass alloy.

^d Aluminum alloy or so-called Duralumin.

conditions described in Section II-A1 and II-A2. The shape of the MP-gear was generated by numerical calculation simulating the hobbing process shown in Fig. 5. The motors were brushless dc (BLDC) motors (Maxon Motor Inc., Switzerland) that are selected for their superior responsiveness.

2) *Material Selections:* The materials of the prototype are listed in Table IV. The CS- and MP-gears are constructed from polyetheretherketone (PEEK), which is a super engineering plastic with high lubricity, machinability, strength, and stability. As the holder is fabricated using polyoxymethylene (POM), the gear-holder contact surfaces require no oiling. The base and housing of the device are constructed from a lightweight and strong aluminum alloy (A2017).

Many parts of the prototype were built from high-performance plastics with high machinability and stable properties because the components of ABENICS have complex shapes, which

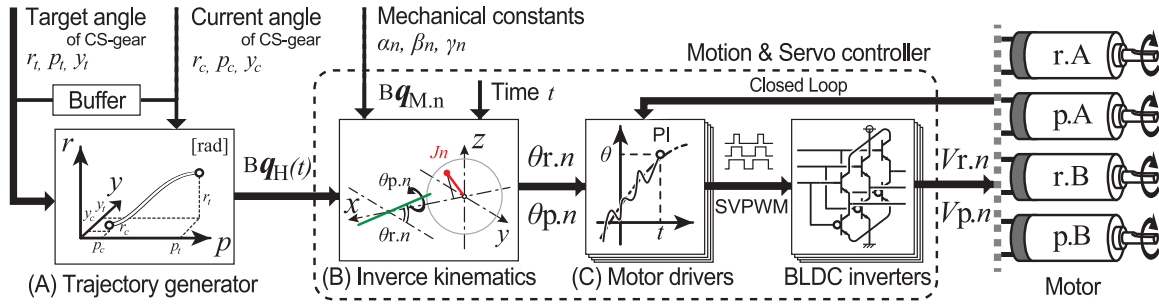


Fig. 15. Schematic of the control system of the new ABENICS, showing the processes (blocks) and flow of information (arrows). The target angles r_t, p_t, y_t of the CS-gear are given by the user. The parameters indicated by the thin arrows are provided by the control system itself. SVPWM denotes the space vector pulsewidth modulation, a field-oriented control method that generates a rotating magnetic field with a three-phase ac voltage $V_{r,n}, V_{p,n}$ via inverters.

TABLE V
MECHANICAL CONSTANTS

Parameter	Perpendicular type	Opposite type	unit
α_A	$\pi/2$	$\pi/2$	rad
β_A	0	0	rad
γ_A	$-\pi/4$	0	rad
α_B	$-\pi/2$	$-\pi/2$	rad
β_B	0	0	rad
γ_B	$3\pi/4$	π	rad

makes estimating problems during prototyping difficult. Construction from strong materials such as metals will also improve the capability of the device.

C. Controller Design

The flow of the prototype control system is shown in Fig. 15. Process (A) provides the trajectory function $B q_H(t)$ using a trajectory generator, and process (B) generates the motor rotation angles $\theta_{r,n}$ and $\theta_{p,n}$ using inverse kinematics. Process (C) is the servo controller that is synchronized with (B). The processing frame composed of (B) and (C) operates at a sufficiently high frequency (1 kHz).

Process (A) interpolates a path between the current orientation r_c, p_c, y_c rad and the target orientation r_t, p_t, y_t rad of the CS-gear with a great circle path and generates a trajectory function $B q_H(t)$ that moves along the path. Process (B) calculates four motor rotation angles $\theta_{r,A}, \theta_{p,A}, \theta_{r,B}, \theta_{p,B}$ from the target orientation $B q_H$ (obtained by inputting the time t s to $B q_H(t)$) and the orientations $B q_{M,A}$ and $B q_{M,B}$ of the driving modules. Process (B) is the described algorithm in Section III and process (C) provides the closed loop control of the four BLDC motors, which is composed of an inverter, a motor, and a rotary encoder. It also provides a proportional-integral (PI) feedback. Note that because of the redundancy of this mechanism, the upper limit of the integral of the driving module B is set to small.

The hardware of processes (A), (B), and (C) is listed below.

- (A) A personal computer (Java Programs).
- (B) NXP-MK64, 32-bit 120-MHz ARM Cortex-M4.
- (C) NXP-MK20, 32-bit 72-MHz ARM Cortex-M4.

Table V gives the values of the mechanical constants α_n, β_n , and γ_n in process (B). The perpendicular-type driving modules in Fig. 14 are perpendicularly aligned. In the opposite-type configuration, driving modules A and B are arranged along a straight line.

V. EXPERIMENT AND DISCUSSION

This section experimentally confirms the characteristics of the ABENICS mechanism mentioned in the introduction, i.e., three RDoF, absence of slippage, and the hypothesis⁷ proposed in Section IV-A. Then, the corresponding results and the practical issues of the mechanism are discussed.

A. Positioning Experiment

Fig. 16 shows the experimental setup to confirm whether the theoretical motion range of the system is achievable in practice. First, the discrete target points were regularly arranged in the configuration space based on the XYZ-Euler angles in Σ_B , within the motion range of the output link. Next, the prototype was operated to reach those points. Finally, the orientation of the output link was measured by a motion-capture system that originally had been coordinated⁸ to match the XYZ-Euler angles in Σ_B of the prototype. If the prototype device can operate in three RDoF, the measured results plotted in the three-dimensional configuration space of r, p , and y should be arranged in a grid.

Both perpendicular- and opposite-type prototypes were employed in this experiment. Based on Table I, the measurement area was set as follows: Roll = ± 90 , pitch = ± 45 (perpendicular type) or ± 30 (opposite type), and yaw = 0 to 270. The target points were set in the area at equal intervals: Roll and pitch = 15 and yaw = 90. To reveal the continuity of positioning, the position measurements were made at each target point, approaching the roll, pitch, and yaw from both the positive and negative sides (± 15 [deg]) taking the six measurements at each point.

⁷The angle between the two driving modules is not limited to 90 [deg].

⁸First, rotate the CS-gear only around the yaw axis and then only around the roll axis to measure the runout of the reference IR marker on the output link extension. Next, adjust the coordinate system of the motion-capture system to eliminate those runouts.

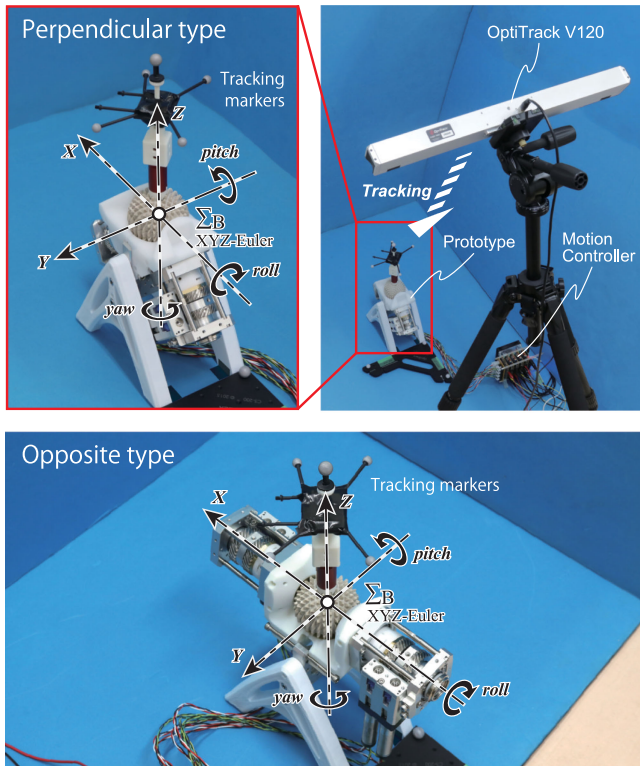


Fig. 16. Experimental setup. The OptiTrack V120 measures the orientation of the tracking marker installed on the prototype's output link. The tracking marker is composed of five infrared reflection markers (IR-markers). The coordinate systems of the prototype's control system and the OptiTrack V120's measurement system are aligned by a calibration process. The base is supported on a pillar fixed to the floor. To eliminate noisy IR reflections, a black tape and a cloth cover the metal parts of the prototype during measurements.

Positions of the tracking marker attached to the output link were measured by the motion-capture system (OptiTrack V120 Trio; Natural Point Inc., Oregon, USA). To obtain the results of one measurement, an average of 120 measurement data during one second was used. The measurement accuracy of this instrument is supplemented by Appendix A.

B. Trajectory Tracking Experiment

This experiment verifies the transient response of the mechanism's prototype as it moves from one orientation to the other: The CS-gear's orientation is measured by following the trajectory of a straight line set in the r , p , y [deg] three-dimensional configuration space. If the tracking of the prototype is good, the measurement points plotted in three-dimensional space should be well linear.

The perpendicular-type prototype was used in this experiment. The measurement method, experimental equipment, and coordinate system were the same as Section V-A.

To set up the measurement trajectory, we prepared reference points (Table VI). The trajectory runs in sequence from P_0 to P_8 . In one straight movement, r , p , and y are each at a constant speed with the same travel time. The fastest rotation is set to 90 [deg/s], while the other two rotation speeds are adjusted to synchronize. Each reference point has a stopping time of 1 s.

TABLE VI
REFERENCE POINTS

	P_0	P_1	P_2	P_3	P_4	P_5	P_6	P_7	P_8
r [deg]	0	-90	-90	90	90	90	90	-90	-90
p [deg]	0	-45	-45	45	-45	45	-45	45	45
y [deg]	0	0	360	0	0	360	360	360	0

The CS-gear orientation was measured with a period of 120 Hz and the results were given by a single continuous tracking test.

C. Experimental Results and Discussion

The experimental results are shown in Figs. 17, 18, and 20. The horizontal, depth, and vertical directions depict the r , p , and y angles, respectively. Fig. 19 displays the serial pictures showing the operation of the perpendicular-type prototype.

1) *Quantitative Discussion of Measurement Results:* From Fig. 17, in both prototype configurations, most of the plotted measurement points were aligned evenly on the orthogonal coordinate system and coincided with their target points. This indicates that the prototypes reached any orientation from any direction. In addition, the plots of the perpendicular and opposite types were similar, suggesting that the capabilities of the ABENICS mechanism were independent of the angle between the two driving modules. Moreover, Fig. 20 shows that the orientation transition of the CS-gear is linear and suggests that the mechanism can follow the trajectory continuously.

A more detailed analysis shows that the error in the repetitive positioning depended on its orientation (e.g., see the error around $r = 90$ [deg], $p = 30$ [deg], and $y = 90$ [deg] in Figs. 17 (a) and 21). This orientation dependence probably results from combining different driving principles, gearing motions, and coupling motions.⁹ The gearing motion uses a differential unit in the driving module, which introduces more error. On the other hand, the coupling motion is a torsional rotation caused by the tooth width of the MP-gear, so its error depends on the tooth width and backlash with CS-gear.¹⁰ The friction caused by the sliding motion depends on the meshing position of the CS-gear and MP-gear. Consequently, the total error due to the composition of the three motions is expected to depend on the relative orientations of CS-gear and MP-gear. According to dial gauge backlash measurements, there was approx. 0.7–0.9 of backlash in gearing motion and approx. 0.8 of backlash in coupling motion. The gearing motion included a backlash of 0.6 caused by the driving module. Note that there are two types of backlash here: 1) Backlash in the driving module and 2) backlash between the CS-gear and MP-gear. In the graphs that show the trajectory tracking, the vibrations in the yaw rotation are noticeable. At $r = 90, -90$ [deg], the output link is horizontal and is affected by gravity, which is also thought to be caused by the backlash. This problem will get better with improvements of design and manufacturing technology. In the near future, we

⁹See Section IV-B.

¹⁰The wider the tooth width of the MP-gear, the greater is the reduction of errors due to backlash with CS-gear.

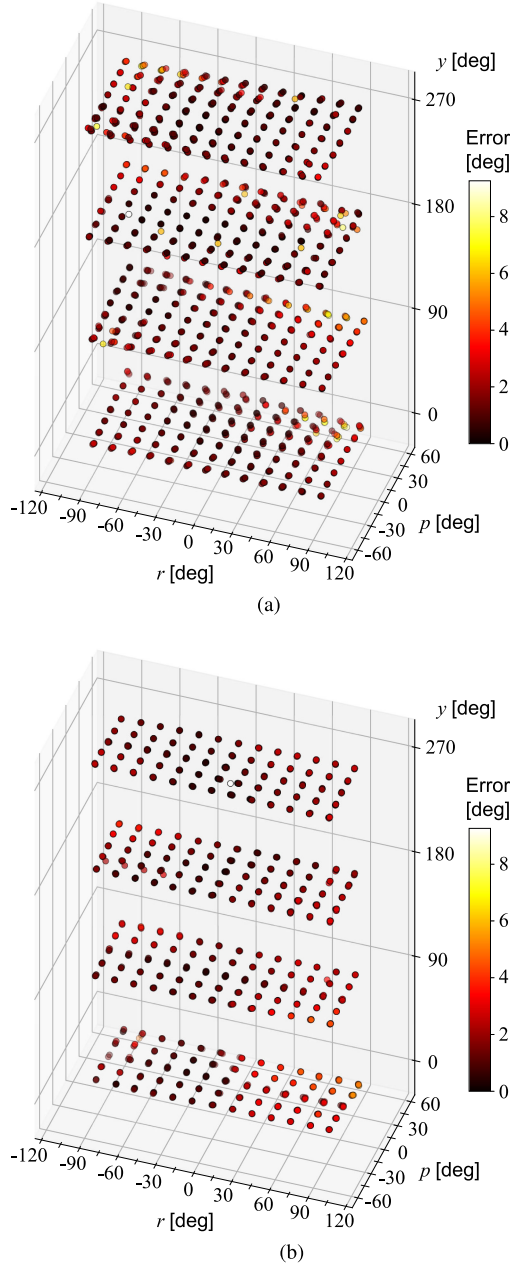


Fig. 17. Scatter diagrams of the results of the positioning experiments. The XYZ-Euler angles (roll r , pitch p , and yaw y degrees) are plotted on the orthogonal coordinate system. The measurement markers reduced the motion range of the opposite type. The colors of the plotted points indicate the magnitudes of the errors between the true and measured values on the orthogonal coordinates. The six measurements at each target point are plotted without averaging each other. All results are plotted in the diagrams and no plots are eliminated. The regular alignment of the plot points shows the correctness of the theory of the proposed mechanism. (a) Perpendicular type (90°). (b) Opposite type (180°).

will establish a method that accurately evaluates these effects by modeling and formulating the underlying mechanism.

2) Qualitative Discussion of Prototype Behavior: Each prototype of ABENICS completed the automated positioning experiment in 3 h. During the experimental runs, the prototypes operated with no catching of gears, meshing failures, or other mechanical problems.

Focusing on the finer behavior, we observed that the roll rotation $\theta_{r,n}$ of the driving module quickly accelerated and decelerated when the MP-gear passed near the poles of the CS-gear. At these moments, the CS-gear vibrated slightly. Referring to (14), which calculates the amount of roll rotation $\theta_{r,n}$ using the inverse tangent function, we find that when $J_{n,y}$ and $J_{n,z}$ are zero, or the position vector J_n reaches the x -axis vicinity at $\Sigma_{M,n}$, $\theta_{r,n}$ must be inverted in a short time. This theory is unrealistic because the true behavior includes a delay. This deviation between the theory and actuality may have caused oscillations in the CS-gear. This problem will be resolved by avoiding or slowing down the singularity area¹¹ that are near the poles of the CS-gear or passing just above the poles without the inversion. Such an avoidance method should be able to apply conventional robotics knowledge.

The singularity in the vicinity of the poles deteriorated the results and presented some control challenges. However, it may provide the torque amplification seen in other robot arms. For example, some rotational components of the CS-gear might be locked strongly without motor torque, just like a toggle mechanism. Because (unlike gimbal mechanisms) the mechanism of ABENICS is free of large moment-of-inertia effects and link interferences, it is effective against these possibilities. Solving the problem of computing the singularity in the control will make these realistic.

Referring to the discussion in Section V-C1, the ABENICS mechanism can potentially achieve accurate, fast, or high-torque configurations by customizing the arrangement of the two driving modules, the holder shape, and the relative positions of the output link and CS-gear. In this way, the mechanism could be adapted to the requirements of a given application. In future work, we plan to evaluate the adaptability of ABENICS mechanism along with the singularity exception control.

D. Discussion on Design Issues

ABENICS has many unique components, such as CS-gear and MP-gear. Although these brought new possibilities, some difficulties are foreseen. Here, the design challenges of this mechanism are discussed.

1) Practical Issues of CS-Gear, MP-Gear, and Holder: This section discusses the practical design and operational issues of CS-gear, MP-gear, and holder.

Of the meshing between the CS-gear and MP-gear, the gearing motion has properties similar to those of normal gear. The backlash between the MP-gear and the CS-gear in the prototype was 0.13–0.34 [deg] in terms of the CS-gear angle, as shown in Appendix A. Since the MP-gear drives the CS-gear with a wide line-contact, its transmission capacity is considered to be large, even if there are some slots in the CS-gear, which is expected due to the other tooth structure. The transmission efficiency is expected to be similar to a normal spur gear, and the forward and backward efficiencies should always be symmetrical. However, near-pole meshing increases sliding contact, so the transmission

¹¹The range of the singularity depends on the circumferential velocity of the CS-gear.

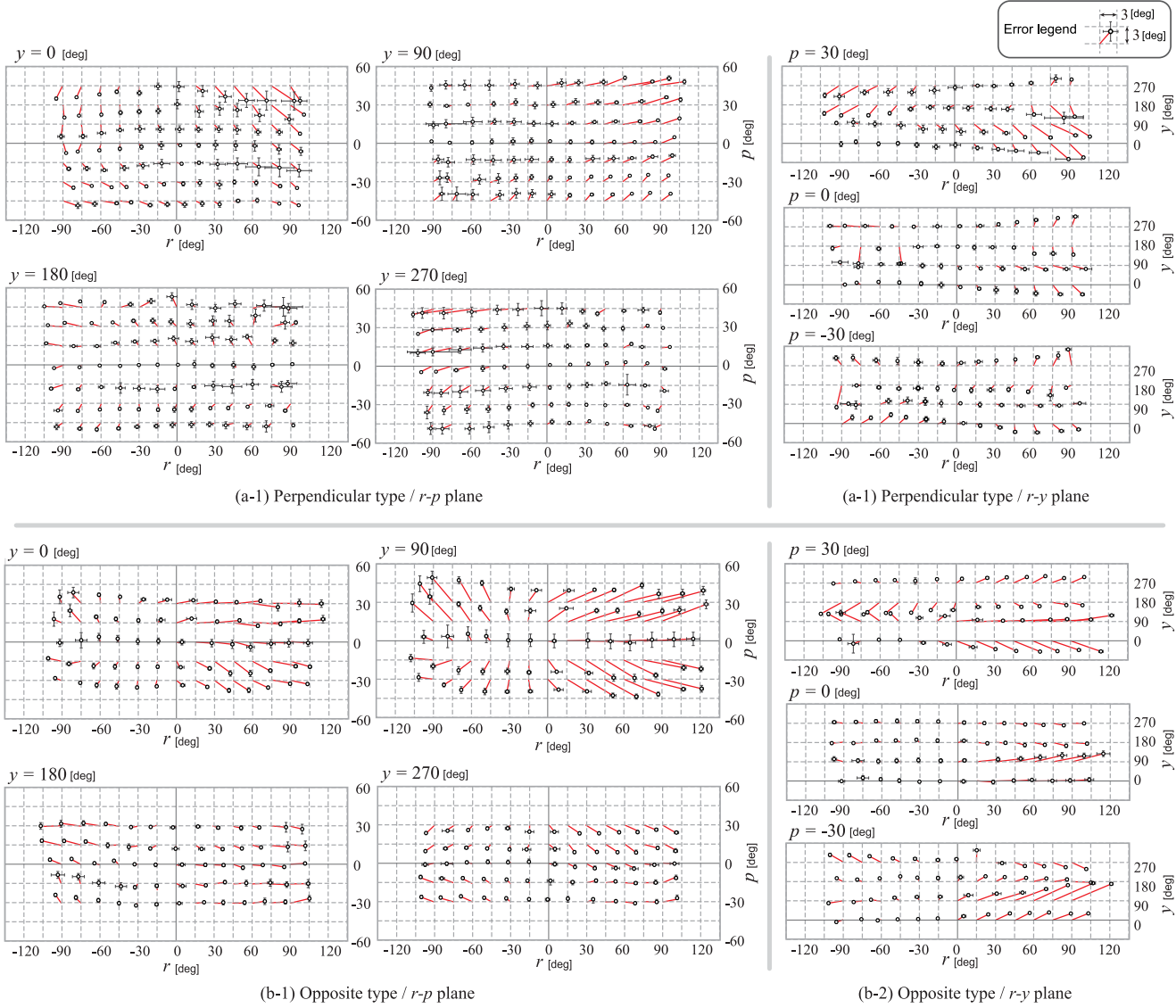


Fig. 18. Average and standard deviation of the results of the positioning experiment. (a-1) and (b-1) are scatter diagrams based on the r - p plane, and (a-2) and (b-2) are based on the r - y plane. Each plotted point is the measured value at the target point of the intersection of the ticks connected by the red lines. These errors and standard deviations are exaggerated, and one square of the graph grid is 3 when reading the values.

efficiency will decrease due to friction. These need to be revealed more in terms of gear engineering.

The sliding motion is a sliding contact behavior that is strongly influenced by friction. Therefore, in practice, the tooth surface should be lubricated with grease, even if it is a resin, to reduce the contact friction with the holder. If there is an error of meshing due to backlash in coupling motion, i.e., an error between the CS-gear and MP-gear tooth line, the notches in the CS-gear may conflict with the MP-gear during the sliding motion. Chamfering to the corner of the CS-/MP-gear teeth will reduce this problem. It is also important to keep a proper backlash.

The distance between the MP-gear and CS-gear is provided by the holder and the driving module. The holder in the current design requires some mechanical compliance to allow for thermal expansion, resin swelling, and fabrication errors to keep the CS-gear on a spherical surface. A small preload is

applied to hold the CS-gear in place and small variations occur depending on the orientation of the CS-gear. In other words, the relative distance between the tooth tips of the CS-gear and the inner surface of the holder does not ideally fluctuate. Since the driving modules installed in the holder also variate with the holder, the distance between the CS-gear and the MP-gear is kept constant. However, in practice, the variation of the relative distance may not be zero. This is a complex problem determined by the distribution of mechanical compliance of the holder, the mounting position of the driving module, the preload, and the amount of fabrication error. Adopting a typical ball joint design approach will contribute to a more appropriate holder design.

2) Manufacturing of MP-Gear and CS-Gear: Establishing a manufacturing method for a CS-gear and MP-gear is one of the biggest challenges. 5-axis machining centers are a viable solution for both metallic and resin materials. On the other hand,

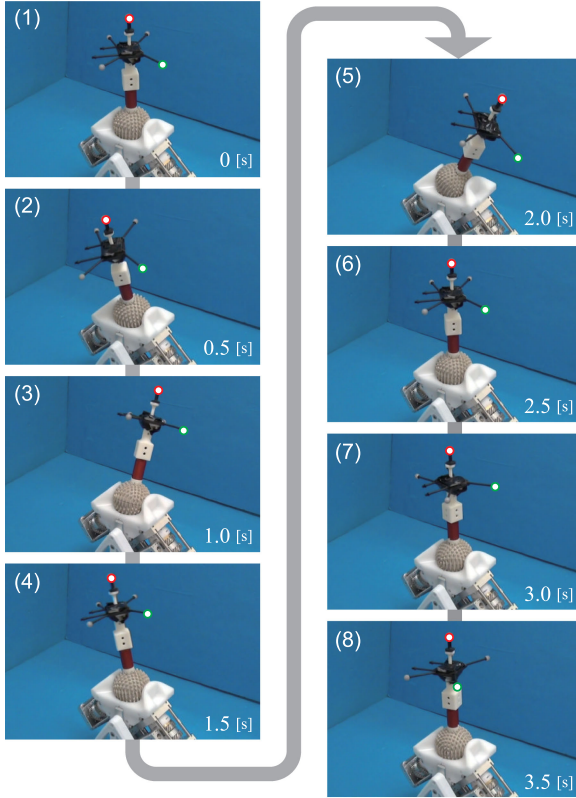


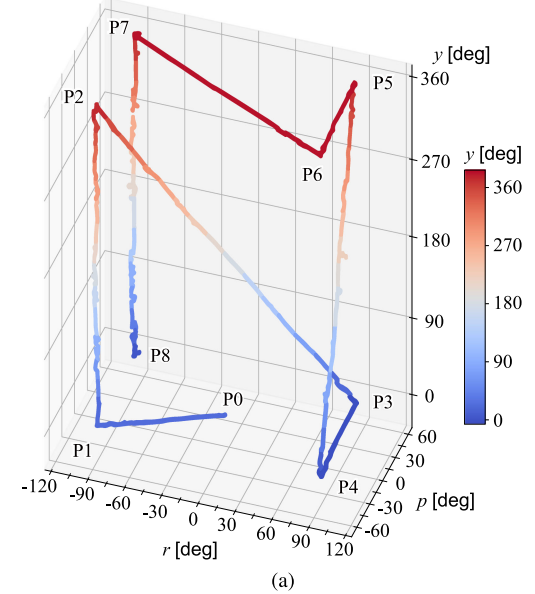
Fig. 19. Movement of the prototype of the new ABENICS in the tracking experiment. To clarify the movement, two infrared reflection markers were characterized with simple red and green circles in these pictures.

although the machining procedure needs to be tested, it may also be possible to lathe-like machining using the CS-gear's linear symmetry. In addition, the MP-gear could be processed such as that in Fig. 5.

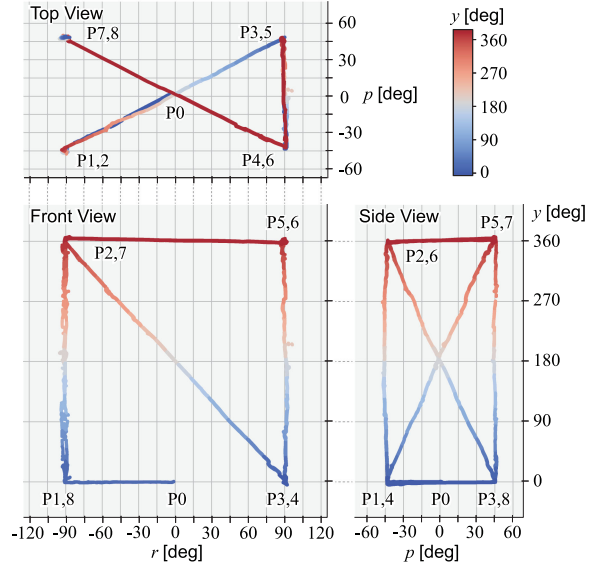
Using a 3D printer is a good way to fabricate this mechanism. Fig. 22 is an early prototype of this project and MP-gears, which were manufactured by stereolithography (SLA) 3D printer for theory validation and are confirmed to work. Also, the MP-gear's shape generation algorithm is already established and the module and number of teeth can be easily changed.

In the case of metal 3D printers, a presence of a rough surface due to the sintering of the metal powder is not suitable for CS-/MP-gear. On the other hand, it is remarkable that combined machining centers and metal 3D printers have emerged in recent years. The problem may be solved by cutting only the tooth contact surface thin in postprocessing.

3) Holder and Range of Motion: The CS-gear of the prototype must be held by a holder. Therefore, if there is an output axis, the range of motion is limited, i.e., there is a tradeoff between the range of motion and stability. Such systems can be found in a friction wheel, a spherical motor, and an ultrasonic system. On the other hand, a linkage or differential mechanism has no such limitations. A comparison of these movable ranges is shown in Table VII [33]. Note that the values of the working ranges in the table depend on the coordinate system of each literature and are not uniform.



(a)



(b)

Fig. 20. Scatterplot of the tracking experiment results. XYZ-Euler angles (roll r , pitch p , and yaw y [deg]) are plotted in the Cartesian coordinate system. The color of the plotted points illustrates the angle of y [deg] and the linearity of the plotted points indicates the transient response of this mechanism. (a) Perspective view. (b) Three-view.

TABLE VII
COMPARISON OF RANGE OF MOTION

Name	Type	θ_1	θ_2	θ_3	[deg]
ABENICS – opposite type	Gear	270	90	360	
Gosselin et al. (Agile Eye) [26]	Linkage	140	140	30	
Birglen et al. (SHaDe) [28]	Linkage	90	45	45	
Hess-Coelho et al. [31]	Linkage	140	140	360	
Hammond et al. [29]	Linkage	180	180	360	
Kaneko et al. [13]	Motor	30	30	360	
Yano et al. [16]	Motor	90	90	360	

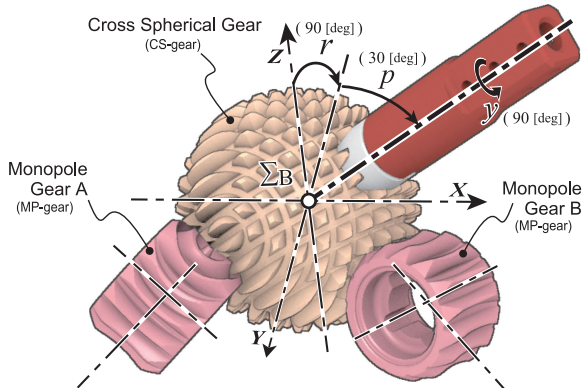


Fig. 21. Schematic diagram of the CS-gear and MP-gears of the perpendicular type prototype at the CS-gear orientation $r = 90$ [deg] $p = 30$ [deg], and $y = 90$ [deg]. Note that the coordinate axes in this figure are in the right-hand coordinate system, i.e., this view is from the minus side of the Z-coordinate. In this case, the roll rotation r of the CS-gear is performed by the gearing motion of both the MP-gears.

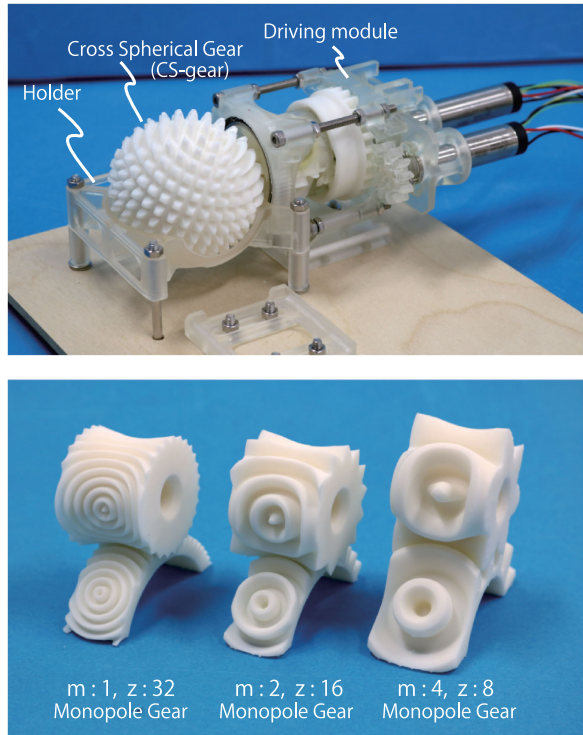


Fig. 22. 3D-printed prototypes and monopole gear (MP-gear) in various modules (m:1, 2, and 4 mm).

One way to increase the range of motion is to remove the bottom part of the opposite type prototype's holder. This reduces the contact area between the CS-gear and the holder. Thus, the stiffness is one of the challenges, but it allows for a range of motion of 360, 90, 360 [deg]. Another way is to design the angle between the driving modules to be small. The prototype's angles are 90 and 180 [deg] but can be placed at a minimum angle of 60 [deg]. If a mechanism to prevent the CS-gear dropout is installed and the overhang is removed from the holder, the

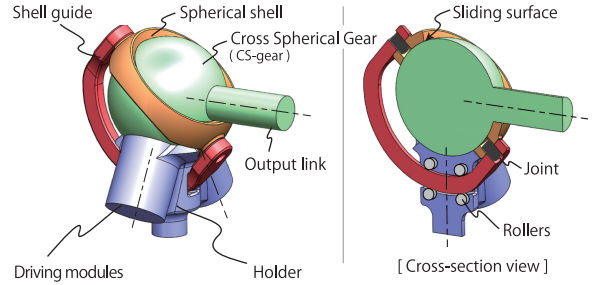


Fig. 23. Illustration of the spherical shell mechanism to hold the CS-gear. This spherical shell is connected to the shell guide by a passive joint. The holder contains two driving modules that have optimized designs. The shell guide is held in place by passive rollers in the holder, which allow the spherical shell to move with the movement of the CS-gear output link, thus allowing for a wide range of motion.

range of motion in this mechanism will be extended to approx. 180, 180, 360 [deg]. We expect that the linkages, magnets, or mobile spherical shells provide auxiliary holding for the CS-gear. Holding the CS-gear in a passive gimbal mechanism is one valid method.¹² However, the singularity of the linkage mechanism will be an issue. On the other hand, a combination of a CS-gear containing a ferromagnetic material and a holder with permanent magnets is an alternative.¹³ In this case, we need to consider the friction caused by magnetic forces and the permissible load of the hand. However, the configuration of the mechanism is relatively simple. In addition, there is one option to hold the CS-gear with a movable spherical shell structure (e.g., Fig. 23). Although many challenges are foreseen in this design, it is possible to hold the CS-gear with surface contact. There are many challenges in designing the holder, but due to the flexibility of its design, we believe ABENICS has a high potential for the near future.

VI. CONCLUSION

This study proposes a new ABENICS based on spherical gear meshing. This mechanism can actively drive three RDoF. First, the study introduced a CS-gear with a quadrature spherical tooth structure and an MP-gear with a unique geometry that allows continuous meshing with the CS-gear. During meshing, the two gear types interacted through gearing, coupling, and sliding motions, allowing a single MP-gear to constrain or drive two RDoF of the CS-gear. This study proposes that the three RDoF of the CS-gear are achieved by driving two MP-gears meshed with two phase-different tooth structures. This idea is reinforced by the mechanistic equivalence of the gear mechanism and a linkage mechanism. It also suggests that the mechanism's capability of ABENICS is independent of the positional arrangement of the MP-gears (driving modules). Moreover, the equivalent linkage led to the forward/inverse kinematics and the torque relationship, and also clarified the actuation redundancy of this mechanism. Strategic distribution of joint torque will make this mechanism more functional. Implementing a developed prototype machine

¹²Some of the spherical motors use similar mechanisms [12]–[14].

¹³Some of the spherical ultrasonic motors use a similar mechanism [9].

and a control algorithm constructed by modeling the mechanism, three RDof are achieved for two different positional arrangements of the MP-gears (perpendicular and opposite type). Results of the positioning and trajectory tracking experiments validated the mechanism of ABENICS and confirmed that the CS-gear can reach any orientation from any direction. Results also revealed a backlash-induced error in the positioning and a singularity of the MP-gear near the poles of the CS-gear. Although the near-polar singularity limited the rotational speed of the CS-gear, this limitation should not significantly reduce the practical applicability of the mechanism because the moment of inertia was smaller than in the gimbal mechanism, and the driving module and output link can be flexibly designed. In addition, it might be possible to amplify the torque near the singularity and lock the orientation of the CS-gear without requiring a motor driving force. Based on the findings from the prototype development and experiments, we discussed practical issues. Advancing the mechanism design and improving the manufacturing accuracy are expected to reduce the backlash and enable miniaturization of the driving module, leading ABENICS to future practical applications.

To investigate the capabilities of ABENICS, we are planning the following tasks.

- 1) Formulate the positional error caused by the placement of components and orientation of the CS-gear.
- 2) Establish control methods at the singularities and verify the torque amplification and locking effects.
- 3) Analyze the meshing between the CS- and MP-gears using theoretical gear technology.
- 4) Develop the control system that provides suitable torque distribution to the joints.

APPENDIX A

CONFIRMATION OF ACCURACY OF THE THREE-DIMENSIONAL MEASURING INSTRUMENT

Here, we check the accuracy of the 3D measuring instrument used in Section V, the Optitrack V120 Trio.

The instrument is a motion-capture system that uses the parallax of multiple *IR* cameras to measure the position and orientation of an object on which an IR reflective marker is placed. The distance and lens coefficients between the cameras are precalibrated. Using three or more markers on the object to be measured, the orientation can be measured with high accuracy. In this article, five markers are used in a redundant arrangement to eliminate incomplete detection due to occlusion.

Fig. 24 is an experimental setup to check the accuracy. It is a two-axis gimbal mechanism with two rotary indexers connected in serial. At the top, the same set of markers as Section V is installed. Because of its axis arrangement, we use ZXZ Euler angles in this measurement and call their rotating axes Z1, X2, and Z3 from the root, i.e., Z1 and X2 are the two indexing machine and corresponding angles, respectively. The angle of the top with the indexer is determined and its accuracy is checked by measuring it with Optitrack. Note that we designed and assembled this mechanism with as much care as possible, but its orthogonality contains uncertainties. Results of the experiment

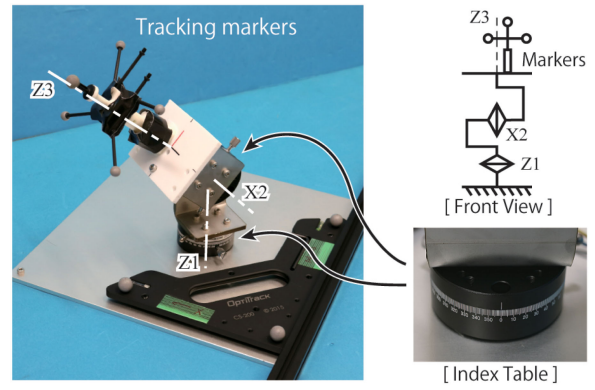


Fig. 24. Experimental setup for measurement accuracy testing. This is a two-axis gimbal with indexers.

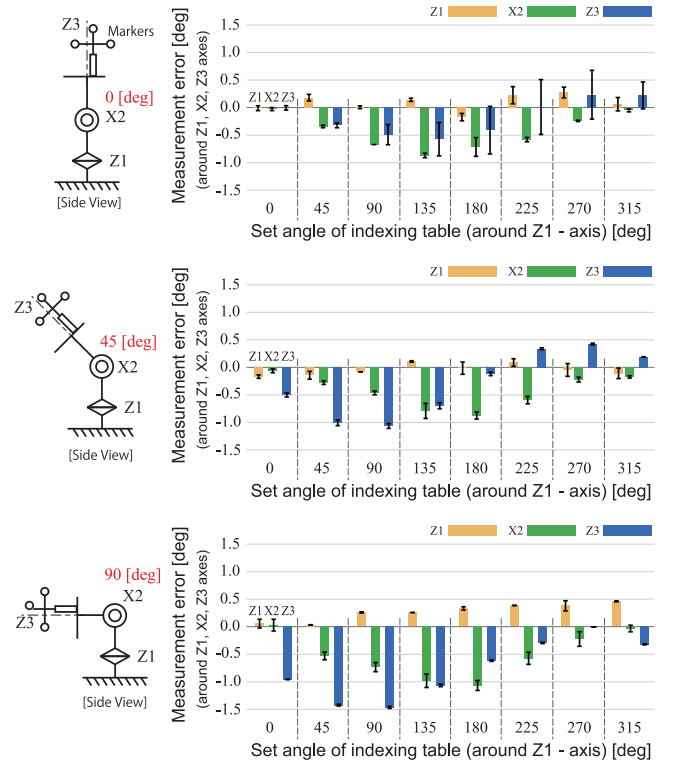


Fig. 25. Accuracy of 3D measuring equipment. Z1 was set at 0–360 in 45 [deg] increments, and X2 was set at 0, 45, and 90 [deg]. The graph is the average of the two measurements and the error bars indicate the difference. In each measurement, the values were taken after standing still for 20 s.

are shown in Fig. 25. Many of the measurement points are within the error of about 1 [deg]. Good repeatability is also confirmed. From the results, we believe that this instrument has sufficient accuracy in measuring orientation.

APPENDIX B CONFIRMATION OF BACKLASH OF THE GEARS

This section supplements the measurement results for the CS-gear, the MP-gear, and the driving module in the prototype. Fig. 26 shows the two patterns used for the measurements. In

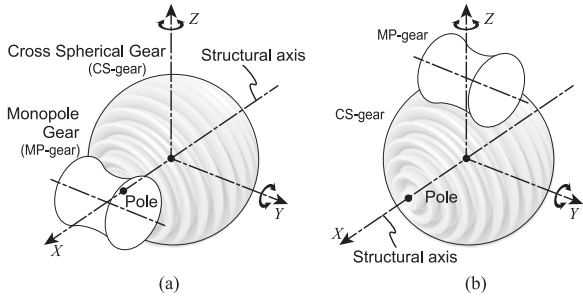


Fig. 26. Schematic diagram of the two types of patterns. (a) Pattern 1. (b) Pattern 2.

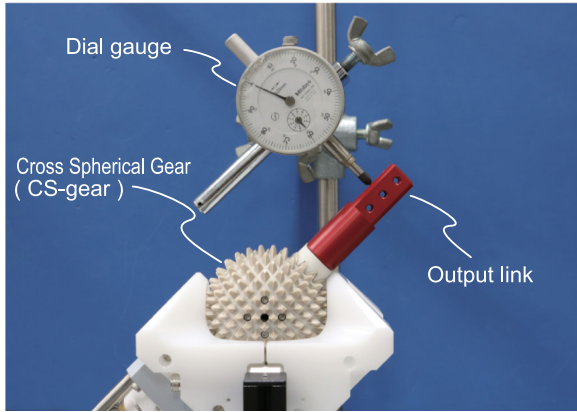


Fig. 27. Measurement of backlash using a dial gauge. The distance from the center of rotation to the measurement point was calculated from the design drawings.

pattern 1, the poles of the CS-gear and the MP-gear are in contact with each other, while pattern 2 is similar to a spur gear meshing. This reveals the following backlash values.

Pattern 1 & Around Y :

Gearing motion with driving module.

Pattern 1 & Around Z :

Gearing motion.

Pattern 2 & Around Y :

Gearing motion with driving module.

Pattern 2 & Around Z :

Coupling motion.

The backlash inside the driving module is also measured.

These backlashes were measured by placing a dial gauge (NO. 2046-08, Mitutoyo Corp.) against the tooth surface of the MP-gear or the output link of the CS-gear (Fig. 27). In this case, one side of the gear train was fixed. The measurements were also made five times each. Note that the MP-gear has a rack shift of -0.1 mm, as shown in Table II. In addition, the distance between the CS-gear and MP-gear's rotational center is 48.0 mm by design but may contain some assembly errors.

Table VIII shows the average Ave and the standard deviation Std of the measured backlash results between the MP-gear and CS-gear. The values in brackets exclude the backlash caused by the driving module. The backlash inside the driving module was

TABLE VIII
RESULTS OF BACKLASH MEASUREMENTS

	Pattern 1		Pattern 2	
	Ave [deg]	Std [deg]	Ave [deg]	Std [deg]
Around Y	0.90 (0.34)	0.013	0.69 (0.13)	0.042
Around Z	0.18	0.041	0.85	0.040

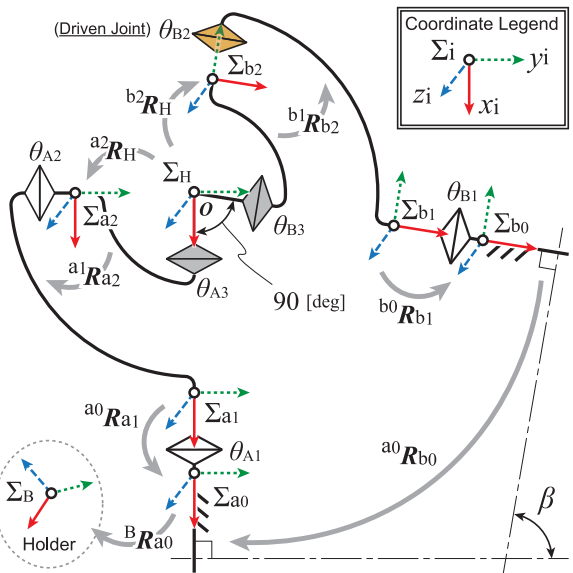


Fig. 28. Detailed skeleton model of the new active ball joint mechanism (ABENICS). The coordinate system of the link Σ_{a0} , Σ_{a1} , Σ_{a2} , Σ_{b0} , Σ_{b1} , Σ_{b2} , the hand (CS-gear) coordinate system Σ_H , and the holder coordinate system Σ_B . The θ is the rotation angle of each joint and β is the angle formed by the two driving modules. R is the coordinate transformation. Since it is a spherical linkage, each coordinate system is actually in the same position as Σ_H .

found to exhibit Ave = 0.57 [deg] and Std = 0.08 in terms of CS-gear. Results show that the gearing motion is dominated by the influence of the driving module and that the coupling motion has less backlash than the gearing motion with the driving module.

APPENDIX C KINEMATICS AND RELATIONAL EQUATIONS

A. Forward Kinematics, Relational Equation, and Jacobian

Define the detailed coordinate system for Fig. 10 as shown in Fig. 28. Because translational movement is not considered here, all coordinate transformations are represented by rotation matrices. The relationship with the rotation angle of the driving module is as follows:

$$\theta_{r,A} = \theta_{A1} \quad \theta_{r,B} = \theta_{B1} \quad (17)$$

$$\theta_{p,A} = -2\theta_{A2} \quad \theta_{p,B} = -2\theta_{B2}. \quad (18)$$

Expressing the rotation matrices around the x , y , and z axes as $R_x(\theta)$, $R_y(\theta)$, and $R_z(\theta)$, respectively, the coordinate transformation in Fig. 10 is as follows:

$${}^{a0}R_{a1} = R_x(\theta_{A1}) \quad (19)$$

$${}^{a1}\mathbf{R}_{a2} = \mathbf{R}_y(\theta_{A2}) \quad (20)$$

$${}^{a2}\mathbf{R}_H = \mathbf{R}_x(\theta_{A3}) \quad (21)$$

$${}^{b0}\mathbf{R}_{b1} = \mathbf{R}_x(\theta_{B1}) \quad (22)$$

$${}^{b1}\mathbf{R}_{b2} = \mathbf{R}_y(\theta_{B2}) \quad (23)$$

$${}^{b2}\mathbf{R}_H = \mathbf{R}_x(\theta_{B3})\mathbf{R}_z(-\pi/2) \quad (24)$$

$${}^{a0}\mathbf{R}_{b0} = \mathbf{R}_z(\beta). \quad (25)$$

Here, for simplicity of expression, it is assumed that ${}^B\mathbf{R}_{a0}$ is the unit matrix by aligning Σ_B with the coordinate system Σ_{a0} of the driving module A.

This closed-link mechanism is a redundant mechanism that realizes three DoF of the CS-gear with four active joints. Thus, they can be considered as three independent active joints and one dependent active joint. Here, we assume that θ_{B2} is the dependent active joint.

The coordinate transformation ${}^B\mathbf{R}_H$ to the hand (CS-gear) in the link chain A is expressed by the following equation, (26) shown at bottom of this page. The S_m and C_m in the equation mean $\sin \theta_m$ and $\cos \theta_m$. Here, to obtain the unknown variable, θ_{A3} , we use the following circularity of closed links:

$${}^{a0}\mathbf{R}_{a1} {}^{a1}\mathbf{R}_{a2} {}^{a2}\mathbf{R}_H = {}^{a0}\mathbf{R}_{b0} {}^{b0}\mathbf{R}_{b1} {}^{b1}\mathbf{R}_{b2} {}^{b2}\mathbf{R}_H. \quad (27)$$

Solving this equation for the passive joint $\mathbf{R}_x(\theta_{B3})$, we obtain the following equation, (28) shown at bottom of this page. Expanding this equation, we obtain

$$\begin{bmatrix} 1 & 0 & 0 \\ 0 & C_{B3} & -S_{B3} \\ 0 & S_{B3} & C_{B3} \end{bmatrix} = \begin{bmatrix} r_{11} & r_{12} & r_{13} \\ r_{21} & r_{22} & r_{23} \\ r_{31} & r_{32} & r_{33} \end{bmatrix} \quad (29)$$

$$r_{11} = 1 = C_{A3}F - S_{A3}(C_{A2}G - S_{A2}H) \quad (30)$$

$$F = C_{A1}C_{B2}S_\beta + C_{A1}C_\beta S_{B1}S_{B2} - C_{B1}S_{A1}S_{B2}$$

$$G = C_{A1}C_{B1}S_{B2} + C_{B2}S_{A1}S_\beta + C_\beta S_{A1}S_{B1}S_{B2}$$

$$H = C_{B2}C_\beta - S_{B2}S_{B1}S_\beta$$

$$r_{12} = 0 = -C_{B2}I - S_{B2}J \quad (31)$$

$$I = C_{A2}C_\beta + S_{A1}S_{A2}S_\beta$$

$$J = C_{A1}C_{B1}S_{A2} - C_{A2}S_{B1}S_\beta + C_\beta S_{A1}S_{A2}S_{B1}$$

$$r_{13} = 0 = -S_{A3}F - C_{A3}(C_{A2}G - S_{A2}H) \quad (32)$$

$$r_{21} = 0 = C_{A3}K - S_{A3}L \quad (33)$$

$$K = C_{A1}C_{B1}C_\beta + S_{A1}S_{B1}$$

$$L = S_{A1}C_{A2}C_{B1}C_\beta - C_{A1}C_{A2}S_{B1} + S_{A2}C_{B1}S_\beta$$

$$r_{22} = C_{B3} = C_{A1}S_{A2}S_{B1} + C_{A2}C_{B1}S_\beta - C_{B1}C_\beta S_{A1}S_{A2} \quad (34)$$

$$r_{23} = -S_{B3} = -C_{A3}L - S_{A3}K \quad (35)$$

$$r_{31} = 0 = C_{A3}M - S_{A3}(C_{A2}N - S_{A2}O) \quad (36)$$

$$M = -C_{A1}C_{B2}C_\beta S_{B1} + C_{A1}S_{B2}S_\beta + S_{A1}C_{B1}C_{B2}$$

$$N = -S_{A1}C_{B2}C_\beta S_{B1} + S_{A1}S_{B2}S_\beta - C_{A1}C_{B1}C_{B2}$$

$$O = S_{B2}C_\beta + C_{B2}S_{B1}S_\beta$$

$$r_{32} = S_{B3} = -C_{A2}O - S_{A2}N \quad (37)$$

$$r_{33} = C_{B3} = -C_{A3}N - S_{A3}M. \quad (38)$$

Here, r_{21} leads to θ_{A3} based on θ_{A1} , θ_{A2} , and θ_{B1}

$$\theta_{A3}$$

$$= \text{atan} \left(\frac{S_{A1}S_{B1} + C_{A1}C_{B1}C_\beta}{-C_{A1}C_{A2}S_{B1} + S_{A2}C_{B1}S_\beta + S_{A1}C_{A2}C_{B1}C_\beta} \right).$$

The forward kinematics can be derived by substituting θ_{A1} , θ_{A2} , and θ_{A3} into (26). Also, r_{12} represents the constraint between θ_{A1} , θ_{A2} , θ_{B1} , and θ_{B2} . Solving this equation for the driven active joint θ_{B2} , we obtain the following equation:

$$\theta_{B2}$$

$$= -\text{atan} \left(\frac{C_{A2}C_\beta + S_{A1}S_{A2}S_\beta}{C_{A1}S_{A2}C_{B1} - C_{A2}S_{B1}S_\beta + S_{A1}S_{A2}S_{B1}C_\beta} \right)$$

where the CS-gear orientation is expressed in terms of XYZ-Euler angles

$$\theta_r = -\text{atan} \left(\frac{S_{B1}C_{A1}S_{A1}S_{A2}^2 + C_{B1}U}{C_{B1}C_{A1}S_{A2}(C_\beta S_{A1}S_{A2} - S_\beta C_{A2}) + S_{B1}V} \right) \quad (39)$$

$$\theta_p$$

$$= \text{asin} (S_{A2}(-C_{A1}C_{A2}S_{B1} + C_{A2}C_{B1}S_{A1}C_\beta + S_{A2}C_{B1}S_\beta)) \quad (40)$$

$$\theta_y = -\text{atan} \left(\frac{S_{A2}}{C_{A2}} (C_{A1}C_{B1}C_\beta + S_{A1}S_{B1}) \right) \quad (41)$$

$${}^B\mathbf{R}_H = {}^B\mathbf{R}_{a0} {}^{a0}\mathbf{R}_{a1} {}^{a1}\mathbf{R}_{a2} {}^{a2}\mathbf{R}_H =$$

$$\begin{bmatrix} C_{A2} & S_{A2}S_{A3} & C_{A3}S_{A2} \\ S_{A1}S_{A2} & C_{A1}C_{A3} - C_{A2}S_{A1}S_{A3} & -C_{A1}S_{A3} - C_{A2}C_{A3}S_{A1} \\ -C_{A1}S_{A2} & C_{A1}C_{A2}S_{A3} + C_{A3}S_{A1} & C_{A1}C_{A2}C_{A3} - S_{A1}S_{A3} \end{bmatrix} \quad (26)$$

$$\mathbf{R}_x(\theta_{B3}) =$$

$$({}^{b1}\mathbf{R}_{b2})^{-1}({}^{b0}\mathbf{R}_{b1})^{-1}({}^{a0}\mathbf{R}_{b0})^{-1} {}^{a0}\mathbf{R}_{a1} {}^{a1}\mathbf{R}_{a2} {}^{a2}\mathbf{R}_H (\mathbf{R}_z(-\pi/2))^{-1} \quad (28)$$

$$U = S_\beta C_{A2} S_{A1} S_{A2} - C_\beta (S_{A1}^2 S_{A2}^2 + 1) \quad (42)$$

$$V = S_{A1}^2 S_{A2}^2 - S_{A2}^2 + 1. \quad (43)$$

Partial differentiation of the above equation at each joint angle yields the Jacobian of the link chain A. Also, the Jacobian of link chain B can be derived by the same procedure.

$$\mathbf{J}_A = \begin{bmatrix} \frac{\partial \theta_r}{\partial \theta_{A1}} & \frac{\partial \theta_r}{\partial \theta_{A2}} & \frac{\partial \theta_r}{\partial \theta_{B1}} \\ \frac{\partial \theta_p}{\partial \theta_{A1}} & \frac{\partial \theta_p}{\partial \theta_{A2}} & \frac{\partial \theta_p}{\partial \theta_{B1}} \\ \frac{\partial \theta_y}{\partial \theta_{A1}} & \frac{\partial \theta_y}{\partial \theta_{A2}} & \frac{\partial \theta_y}{\partial \theta_{B1}} \end{bmatrix} = \begin{bmatrix} j_{11} & j_{12} & j_{13} \\ j_{21} & j_{22} & j_{23} \\ j_{31} & j_{32} & j_{33} \end{bmatrix}. \quad (44)$$

B. Inverse Kinematics

The relationship from the coordinate system of the base (holder) to the orientation of the hand (CS-gear) can be expressed in each of the link chains A and B as follows. Here, ${}^B\mathbf{R}_H$ is a known value

$${}^B\mathbf{R}_H = {}^B\mathbf{R}_{a0} {}^{a0}\mathbf{R}_{a1} {}^{a1}\mathbf{R}_{a2} {}^{a2}\mathbf{R}_H \quad (45)$$

$${}^B\mathbf{R}_H = {}^B\mathbf{R}_{a0} {}^{a0}\mathbf{R}_{b0} {}^{b0}\mathbf{R}_{b1} {}^{b1}\mathbf{R}_{b2} {}^{b2}\mathbf{R}_H. \quad (46)$$

Using (19)–(25) and arranging the unknown components on the left-hand side, each equation can be expressed as follows:

$$\mathbf{R}_x(\theta_{A1}) \mathbf{R}_y(\theta_{A2}) \mathbf{R}_x(\theta_{A3}) = ({}^B\mathbf{R}_{A0})^{-1} {}^B\mathbf{R}_H \quad (47)$$

$$\begin{aligned} \mathbf{R}_x(\theta_{B1}) \mathbf{R}_y(\theta_{B2}) \mathbf{R}_x(\theta_{B3}) = \\ (\mathbf{R}_z(\beta))^{-1} ({}^B\mathbf{R}_{A0})^{-1} {}^B\mathbf{R}_H (\mathbf{R}_z(-\pi/2))^{-1}. \end{aligned} \quad (48)$$

By expanding both sides of each equation, the following equations are obtained. However, since the right-hand side is a known component, its detailed derivation is omitted. Now, focusing on the *1, *2, and *3 components of (49) and (50) shown at bottom of this page, we obtain the following equations:

$$\theta_{A1} = \text{atan} \left(-\frac{r_{a21}}{r_{a31}} \right) \quad \theta_{B1} = \text{atan} \left(-\frac{r_{b21}}{r_{b31}} \right) \quad (51)$$

$$\theta_{A2} = \text{acos} (r_{a11}) \quad \theta_{B2} = \text{acos} (r_{b11}) \quad (52)$$

$$\theta_{A3} = \text{atan} \left(\frac{r_{a12}}{r_{a13}} \right) \quad \theta_{B3} = \text{atan} \left(\frac{r_{b12}}{r_{b13}} \right). \quad (53)$$

If the CS-gear orientation is defined by the XYZ-Euler angles, then ${}^B\mathbf{R}_H = R_x(r)R_y(p)R_z(y)$. Therefore, the specific angle for each joint is given by

$$\theta_{A1} = \text{atan} \left(\frac{C_r S_y + C_y S_p S_r}{C_r C_y S_p - S_r S_y} \right) \quad (54)$$

$$\theta_{A2} = \text{acos} (C_p C_y) \quad (55)$$

$$\theta_{A3} = -\text{atan} \left(\frac{C_p S_y}{S_p} \right) \quad (56)$$

$$\theta_{B1} = -\text{atan} \left(\frac{C_y C_\beta C_r + S_y (S_\beta C_p - C_\beta S_p S_r)}{C_r S_p S_y + C_y S_r} \right) \quad (57)$$

$$\theta_{B2} = \text{acos} (C_y C_r S_\beta - S_y (C_\beta C_p + S_\beta S_p S_r)) \quad (58)$$

$$\theta_{B3} = \text{atan} \left(\frac{C_y (C_\beta C_p + S_\beta S_p S_r) + S_y S_\beta C_r}{-C_\beta S_p + S_\beta C_p S_r} \right). \quad (59)$$

C. Inverse Jacobian and Torque Equations

Since this mechanism is a redundant closed-link mechanism, antagonistic or superimposed torques are expected to exist inside the mechanism. In this section, the relational equations are first derived from hand velocity to joint angular velocity. Next, the torque equation is derived using the principle of virtual work. To simplify the equation, $\beta = 90^\circ$

is used here.

The inverse Jacobian \mathbf{J}_A^{-1} and \mathbf{J}_B^{-1} in the link chain A and B are calculated by substituting (54)–(59) into the following equations:

$$\begin{aligned} \mathbf{J}_A^{-1} &= \begin{bmatrix} \frac{\partial \theta_{A1}}{\partial \theta_r} & \frac{\partial \theta_{A1}}{\partial \theta_p} & \frac{\partial \theta_{A1}}{\partial \theta_y} \\ \frac{\partial \theta_{A2}}{\partial \theta_r} & \frac{\partial \theta_{A2}}{\partial \theta_p} & \frac{\partial \theta_{A2}}{\partial \theta_y} \\ \frac{\partial \theta_{A3}}{\partial \theta_r} & \frac{\partial \theta_{A3}}{\partial \theta_p} & \frac{\partial \theta_{A3}}{\partial \theta_y} \end{bmatrix} = \begin{bmatrix} ja_{11} & ja_{12} & ja_{13} \\ ja_{21} & ja_{22} & ja_{23} \\ ja_{31} & ja_{32} & ja_{33} \end{bmatrix} \\ ja_{11} &= 1, \quad ja_{12} = \frac{C_p C_y S_y}{C_p^2 C_y^2 - 1}, \quad ja_{13} = \frac{S_p}{-C_p^2 C_y^2 + 1} \\ ja_{21} &= 0, \quad ja_{22} = \frac{C_y S_p}{\sqrt{-C_p^2 C_y^2 + 1}}, \quad ja_{23} = \frac{C_p S_y}{\sqrt{-C_p^2 C_y^2 + 1}} \end{aligned}$$

$$\begin{aligned} &\begin{bmatrix} C_{A2}|^{*2} & S_{A2} S_{A3}|^{*3} & C_{A3} S_{A2}|^{*3} \\ S_{A1} S_{A2}|^{*1} & C_{A1} C_{A3} - C_{A2} S_{A1} S_{A3} - C_{A1} S_{A3} - C_{A2} C_{A3} S_{A1} \\ -C_{A1} S_{A2}|^{*1} & C_{A1} C_{A2} S_{A3} + C_{A3} S_{A1} & C_{A1} C_{A2} C_{A3} - S_{A1} S_{A3} \end{bmatrix} \\ &= \begin{bmatrix} r_{a11}|^{*2} & r_{a12}|^{*3} & r_{a13}|^{*3} \\ r_{a21}|^{*1} & r_{a22} & r_{a23} \\ r_{a31}|^{*1} & r_{a32} & r_{a33} \end{bmatrix} \end{aligned} \quad (49)$$

$$\begin{aligned} &\begin{bmatrix} C_{B2}|^{*2} & S_{B2} S_{B3}|^{*3} & C_{B3} S_{B2}|^{*3} \\ S_{B1} S_{B2}|^{*1} & C_{B1} C_{B3} - C_{B2} S_{B1} S_{B3} - C_{B1} S_{B3} - C_{B2} C_{B3} S_{B1} \\ -C_{B1} S_{B2}|^{*1} & C_{B1} C_{B2} S_{B3} + C_{B3} S_{B1} & C_{B1} C_{B2} C_{B3} - S_{B1} S_{B3} \end{bmatrix} \\ &= \begin{bmatrix} r_{b11}|^{*2} & r_{b12}|^{*3} & r_{b13}|^{*3} \\ r_{b21}|^{*1} & r_{b22} & r_{b23} \\ r_{b31}|^{*1} & r_{b32} & r_{b33} \end{bmatrix} \end{aligned} \quad (50)$$

$$ja_{31} = 0, \quad ja_{32} = -\frac{S_y}{C_p^2 C_y^2 - 1} \quad ja_{33} = -\frac{C_y \tan(\theta_p)}{S_y^2 + \tan^2(\theta_p)} \quad (60)$$

$$\mathbf{J}_B^{-1} = \begin{bmatrix} \frac{\partial \theta_{B1}}{\partial \theta_r} & \frac{\partial \theta_{B1}}{\partial \theta_p} & \frac{\partial \theta_{B1}}{\partial \theta_y} \\ \frac{\partial \theta_{B2}}{\partial \theta_r} & \frac{\partial \theta_{B2}}{\partial \theta_p} & \frac{\partial \theta_{B2}}{\partial \theta_y} \\ \frac{\partial \theta_{B3}}{\partial \theta_r} & \frac{\partial \theta_{B3}}{\partial \theta_p} & \frac{\partial \theta_{B3}}{\partial \theta_y} \end{bmatrix} = \begin{bmatrix} jb_{11} & jb_{12} & jb_{13} \\ jb_{21} & jb_{22} & jb_{23} \\ jb_{31} & jb_{32} & jb_{33} \end{bmatrix}$$

$$jb_{11} = \frac{C_p S_y (C_r C_y S_y - S_p S_r S_y)}{F}$$

$$jb_{12} = \frac{S_y (C_r S_y + C_y S_p S_r)}{F}$$

$$jb_{13} = -\frac{C_p S_r}{F}$$

$$jb_{21} = \frac{(C_r S_p S_y + C_y S_r)}{G}$$

$$jb_{22} = \frac{C_p S_r S_y}{G}$$

$$jb_{23} = \frac{C_r S_y + C_y S_p S_r}{G}$$

$$jb_{31} = -\frac{C_p S_y}{H} \quad jb_{32} = \frac{S_r (C_r S_p S_y + C_y S_r)}{H}$$

$$jb_{33} = \frac{C_p S_r (C_r C_y - S_p S_r S_y)}{H} \quad (61)$$

$$F = C_p^2 S_y^2 + (C_r S_p S_y + C_y S_r)^2$$

$$H = C_p^2 S_r^2 + (C_r S_y + C_y S_p S_r)^2$$

$$G = \sqrt{-(-C_r C_y + S_p S_r S_y)^2 + 1}.$$

Based on the principle of virtual work and using $(\mathbf{J}_A^{-1})^T$ and $(\mathbf{J}_B^{-1})^T$, an expression is obtained to derive the torque $\tau_{out.A}$, $\tau_{out.B}$ at the hand end in each link chain from the torque $\tau_{in.A}$, $\tau_{in.B}$ at the joints

$$\tau_{out.A} = (\mathbf{J}_A^{-1})^T \cdot \tau_{in.A} \quad (62)$$

$$\tau_{out.B} = (\mathbf{J}_B^{-1})^T \cdot \tau_{in.B}. \quad (63)$$

Here, since the torque at the hand tip is $\tau_{out} = \tau_{out.A} + \tau_{out.B}$, the formula for the relationship between the torque at the hand tip and at the joint is derived as follows:

$$\tau_{out} = (\mathbf{J}_A^{-1})^T \cdot \tau_{in.A} + (\mathbf{J}_B^{-1})^T \cdot \tau_{in.B} \quad (64)$$

$$\begin{bmatrix} \tau_{out.r} \\ \tau_{out.p} \\ \tau_{out.y} \end{bmatrix} = (\mathbf{J}_A^{-1})^T \cdot \begin{bmatrix} \tau_{in.A1} \\ \tau_{in.A2} \\ \tau_{in.A3} \end{bmatrix} + (\mathbf{J}_B^{-1})^T \cdot \begin{bmatrix} \tau_{in.B1} \\ \tau_{in.B2} \\ \tau_{in.B3} \end{bmatrix}. \quad (65)$$

Assuming that the passive joint torques are $\tau_{in.A3} = 0$ and $\tau_{in.B3} = 0$, the following three more specific torque equations can be obtained:

$$\tau_{out.r} = ja_{11} \cdot \tau_{in.A1} + jb_{11} \cdot \tau_{in.B1} + jb_{21} \cdot \tau_{in.B2} \quad (66)$$

$$\tau_{out.p} = ja_{12} \cdot \tau_{in.A1} \quad (67)$$

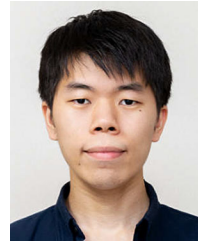
$$\begin{aligned} &+ ja_{22} \cdot \tau_{in.A2} + jb_{12} \cdot \tau_{in.B1} + jb_{22} \cdot \tau_{in.B2} \\ \tau_{out.y} = ja_{13} \cdot \tau_{in.A1} &+ ja_{23} \cdot \tau_{in.A2} + jb_{13} \cdot \tau_{in.B1} + jb_{23} \cdot \tau_{in.B2}. \end{aligned} \quad (68)$$

By solving this system of simultaneous equations, we can obtain $\tau_{in.A1}$, $\tau_{in.A2}$, $\tau_{in.B1}$, and $\tau_{in.B2}$ that satisfy the target hand (CS-gear) torque. This means that antagonistic torques can be caused between the active joints depending on the orientation, but on the other hand, the torques can be superimposed on each other to increase the stiffness. In addition, using the passive joint torques $\tau_{in.A3}$ and $\tau_{in.B3}$ as the effect of friction in the sliding motion, a more accurate calculation is possible.

REFERENCES

- [1] J. Z. A. Deninson, "Vericle," U.S. Patent US1928412 A, Jan. 1930.
- [2] W. H. Isely, "Control apparatus," U.S. Patent US3267755 A, Apr. 1964.
- [3] A. Kimura, M. Matsuzaki, A. Tanaka, and M. Inoue, "Lens frame supporting mechanism," U.S. Patent US5502598 A, Nov. 1992.
- [4] S. Keshtkar, J. A. Moreno, H. Kojima, and E. Hernández, "Design concept and development of a new spherical attitude stabilizer for small satellites," *IEEE Access*, vol. 6, pp. 57 353–57 365, 2018.
- [5] J. Robinson, J. Holland, M. Hayes, and R. Langlois, "Velocity-level kinematics of the atlas spherical orienting device using omni-wheels," *Trans. Can. Soc. Mech. Eng.*, vol. 29, no. 4, pp. 691–700, 2005.
- [6] M. Kumagai and T. Ochiai, "Development of a robot balanced on a ball—Application of passive motion to transport" in *Proc. IEEE Int. Conf. Robot. Automat.*, 2009, pp. 4106–4111.
- [7] Y. Tsumaki, T. Ohgi, and A. Niizuma, "A spherical haptic interface with unlimited workspace," *Int. J. Smart Sens. Intell. Syst.*, vol. 3, no. 3, pp. 691–700, 2010.
- [8] S. Toyama, S. Sugitani, ZhangGuoqiang, Y.Miyatai, and K.Nakamura, "Multi degree of freedom spherical ultrasonic motor," in *Proc. IEEE Int. Conf. Robot. Automat.*, vol. 3, 1995, pp. 2935–2940.
- [9] T. Ueno, C. Saito, N. Imaizumi, and T. Higuchi, "Miniature spherical motor using bimetal of magnetostrictive materials," in *Proc. 50th Jpn. Joint Autom. Control Conf.*, vol. 50, 2007, pp. 18–18.
- [10] B. Lu and M. Aoyagi, "Examination of an outer-rotor-type multidegree-of-freedom spherical ultrasonic motor," in *Proc. 15th Int. Conf. Elect. Machines Syst.*, 2012, pp. 1–5.
- [11] H. Paku and K. Uchiyama, "Satellite attitude control system using a spherical reaction wheel," *Appl. Mechanics Materials*, vol. 798, pp. 256–260, Nov. 2015.
- [12] F. C. Williams, E. R. Laithwaite, and J. F. Eastham, "Development and design of spherical induction motors," *Proc. IEE - Part A: Power Eng.*, vol. 106, no. 30, pp. 471–484, 1959.
- [13] K. Kaneko, I. Yamada, and K. Itao, "A spherical DC servo motor with three degrees of freedom," *J. Dyn. Syst., Meas., Control*, vol. 111, no. 3, pp. 398–402, Sep. 1989.
- [14] K. Lee and C. Kwan, "Design concept development of a spherical stepper for robotic applications," *IEEE Trans. Robot. Automat.*, vol. 7, no. 1, pp. 175–181, Feb. 1991.
- [15] K. Lee, H. Son, and J. Joni, "Concept development and design of a spherical wheel motor (SWM)," in *Proc. IEEE Int. Conf. Robot. Automat.*, 2005, pp. 3652–3657.
- [16] T. Yano, T. Suzuki, M. Sonoda, and M. Kaneko, "Basic characteristics of the developed spherical stepping motor," in *Proc. IEEE/RSJ Int. Conf. Intell. Robots Syst. Human Environ. Friendly Robots High Intell. Emotional Quotients*, vol. 3, 1999, pp. 1393–1398.
- [17] A. Gofuku, R. Sasaki, T. Yano, Y. Wada, and M. Shibata, "Development of a spherical stepping motor rotating around six axes," *Int. J. Appl. Electromagnetics Mechanics*, vol. 39, no. 1/4, pp. 905–911, 2012.
- [18] M. Kumagai and R. L. Hollis, "Development and control of a three DOF spherical induction motor," in *Proc. IEEE Int. Conf. Robot. Automat.*, 2013, pp. 1528–1533.
- [19] H. Kim, H. Kim, D. Ahn, and D. Gweon, "Design of a new type of spherical voice coil actuator," *Sensors Actuators A: Phys.*, vol. 203, pp. 181–188, 2013.

- [20] U. Nagarajan, G. Kantor, and R. Hollis, "The ballbot: An omnidirectional balancing mobile robot," *Int. J. Robot. Res.*, vol. 33, no. 6, pp. 917–930, 2014.
- [21] H. Y. Kim, H. Kim, D. Gweon, and J. Jeong, "Development of a novel spherical actuator with two degrees of freedom," *IEEE/ASME Trans. Mechatronics*, vol. 20, no. 2, pp. 532–540, 2015.
- [22] J. F. P. Fernandes and P. J. C. Branco, "The shell-like spherical induction motor for low-speed traction: Electromagnetic design, analysis, and experimental tests," *IEEE Trans. Ind. Electron.*, vol. 63, no. 7, pp. 4325–4335, Jul. 2016.
- [23] H. Li and T. Li, "End-effect magnetic field analysis of the Halbach array permanent magnet spherical motor," *IEEE Trans. Magn.*, vol. 54, no. 4, pp. 1–9, Apr. 2018.
- [24] K. N. Souza, R. S. Pontes, A. P. Oliveira, and G. A. Barreto, "Design and control of a three-coil permanent magnet spherical motor," *Energies*, vol. 11, no. 8, 2018, Art. no. 2009.
- [25] F. Chai, L. Gan, and L. Chen, "A novel tiered type permanent magnet spherical motor and its rotor orientation measurement principle," *IEEE Access*, vol. 8, pp. 15 303–15 312, 2020.
- [26] C. M. Gosselin, E. St Pierre, and M. Gagne, "On the development of the agile eye," *IEEE Robot. Automat. Mag.*, vol. 3, no. 4, pp. 29–37, Dec. 1996.
- [27] P. Vischer and R. Clavel, "Argos: A novel 3-DOF parallel wrist mechanism," *Int. J. Robot. Res.*, vol. 19, no. 1, pp. 5–11, 2000.
- [28] L. Birglen, C. Gosselin, N. Pouliot, B. Monsarrat, and T. Laliberte, "SHaDe, a new 3-DOF haptic device," *IEEE Trans. Robot. Automat.*, vol. 18, no. 2, pp. 166–175, Apr. 2002.
- [29] T. A. Hess-Coelho, "A redundant parallel spherical mechanism for robotic wrist applications," *J. Mech. Des.*, vol. 129, no. 8, pp. 891–895, Sep. 2006.
- [30] Y. Yu, Y. Narita, Y. Harada, and T. Nakao, "Research of 3-DOF active rotational ball joint," in *Proc. IEEE/RSJ Int. Conf. Intell. Robots Syst.*, 2009, pp. 5153–5158.
- [31] F. L. Hammond, R. D. Howe, and R. J. Wood, "Dexterous high-precision robotic wrist for micromanipulation," in *Proc. 16th Int. Conf. Adv. Robot.*, 2013, pp. 1–8.
- [32] Y. Kim, J. Kim, and W. Jang, "Quaternion joint: Dexterous 3-DOF joint representing quaternion motion for high-speed safe interaction," in *Proc. IEEE/RSJ Int. Conf. Intell. Robots Syst.*, 2018, pp. 935–942.
- [33] N. M. Bajaj, A. J. Spiers, and A. M. Dollar, "State of the art in artificial wrists: A review of prosthetic and robotic wrist design," *IEEE Trans. Robot.*, vol. 35, no. 1, pp. 261–277, Feb. 2019.
- [34] A. Alan, "Remote-control manipulators," U.S. Patent US3231098 A, May. 1963.
- [35] L. Tsai, "The kinematics of spatial robotic bevel-gear trains," *IEEE J. Robot. Autom.*, vol. 4, no. 2, pp. 150–156, Apr. 1988.
- [36] N. P. Belfiore, "An atlas of remote actuated bevel gear wrist mechanisms of up to nine links," *Int. J. Robot. Res.*, vol. 12, no. 5, pp. 448–459, 1993.
- [37] A. Albers, S. Brudniok, and W. Burger, "Design and development process of a humanoid robot upper body through experimentation," in *Proc. 4th IEEE/RAS Int. Conf. Humanoid Robots*, vol. 1, 2004, pp. 77–92.
- [38] K. A. Wyrobek, E. H. Berger, H. F. M. Van der Loos, and J. K. Salisbury, "Towards a personal robotics development platform: Rationale and design of an intrinsically safe personal robot," in *Proc. IEEE Int. Conf. Robot. Automat.*, 2008, pp. 2165–2170.
- [39] K. Nakayama, "Wrist driving structure part of industrial robot having degree of freedom of rotation triaxiality," *JP Pat. JP2014237206 A*, Jun. 2013.
- [40] K. C. Melgoza, "Spherical robotic shoulder joint," U.S. Patent US5533418 A, Dec. 1994.
- [41] P. Vasta, M. Franco, and M. Thomas, "Fixation device and multiple-axis joint for a fixation device," U.S. Patent US8377060B2, Nov. 2009.
- [42] K. Tadakuma et al., "Study on the omnidirectional driving gear mechanism," in *Proc. IEEE Int. Conf. Robot. Automat.*, 2012, pp. 3531–3532.
- [43] R. Tadakuma, K. Tadakuma, and E. F. M. Arimie, "Study on omnidirectional driving mechanisms to realize holonomic power transmission," in *Proc. Int. Symp. Micromechatronics Human Sci.*, 2013, pp. 1–5.
- [44] K. Tadakuma, H. Saito, K. Abe, S. Hao, and R. Tadakuma, "Study on mechanism of spherical omnidirectional driving gearwith two degrees of freedom," *J. Robot. Soc. Jpn.*, vol. 36, no. 9, pp. 627–638, 2018.
- [45] K. Abe, G. Matsui, K. Tadakuma, M. Yamano, and R. Tadakuma, "Development of the omnidirectional transporting table based on omnidirectional driving gear," *Adv. Robot.*, vol. 34, no. 6, pp. 358–374, 2020.
- [46] C. H. J. De, "Universal joint," U.S. Patent US2171059 A, Mar. 1938.
- [47] W. W. Weible, "Double cardan universal joint with improved centering means," U.S. Patent US4509932 A, Apr. 1981.
- [48] L. Ting and P. Cunyun, "On grinding manufacture technique and tooth contact and stress analysis of ring-involute spherical gears," *Mechanism Mach. Theory*, vol. 44, no. 10, pp. 1807–1825, 2009.
- [49] H. Hong, "Involute non-ring continuous teeth spherical gear transmission mechanism," U.S. Patent US20150128734A1, Oct. 2013.



Kazuki Abe (Member, IEEE) received the B.Eng. degree in mechanical engineering and the Ph.D. degree in mechanical system engineering from Yamagata University, Yamagata, Japan, in 2016 and 2021, respectively.

His research interests include mechanisms, control algorithms, and embedded technology for robots and mechatronics systems.

Dr. Abe is a member of the The Robotics Society of Japan (RSJ) and The Japan Society of Mechanical Engineers (JSME).



Kenjiro Tadakuma (Member, IEEE) received the Ph.D. degree in mechanical and aerospace engineering from the Tokyo Institute of Technology, Tokyo, Japan, in 2007.

He is currently an Associate Professor with the Graduate School of Information Sciences, Tohoku University, Sendai, Japan. His research interests include mechanisms, omnidirectional mobile robots, and rescue robots.

Dr. Tadakuma is a Member of the Robotics Society of Japan (RSJ), the Japan Society of Mechanical Engineers (JSME), the Society of Instrument and Control Engineers (SICE), the Japan Society for Design Engineering (JSDE), and the Japanese Society for Regenerative Medicine (JSRM). He was the recipient of the Young Scientist's Prize for the Commendation of Science and Technology by the Minister of Education, Culture, Sports, Science and Technology (MEXT) in 2011.



Riichiro Tadakuma (Member, IEEE) received the B.S. and M.Eng. degree in mechanical and aerospace engineering from the Tokyo Institute of Technology, Tokyo, Japan, in 2000 and 2002, respectively. He received the Ph.D. degree in advanced interdisciplinary studies from the University of Tokyo, Tokyo, in 2005.

He was a Research Fellow with the Japan Society for the Promotion of Science, from 2003 to 2005. He was also a Research Fellow with the University of Tokyo through the fellowship of the Japan Science and Technology Agency, from 2005 to 2006. From 2006 to 2008, he was a Postdoctoral Research Fellow with the Japan Society for the Promotion of Science. He was a Postdoctoral Research Fellow with the LAAS/CNRS, Toulouse, France, from 2009 to 2010. From 2010 to 2013, he was an Assistant Professor with Yamagata University, Yamagata, Japan, and an Associate Professor, in April 2013. His research interests include the development of robotic mechanisms, actuators, and manipulation.